UCLA
UCLA Previously Published Works

Title

Biogeochemical Consequences of Nonvertical Methane Transport in Sediment Offshore Northwestern Svalbard

Permalink

https://escholarship.org/uc/item/8gf068cj

Journal

Journal of Geophysical Research Biogeosciences, 125(3)

ISSN

2169-8953

Authors

Treude, T
Krause, S
Steinle, L
et al.

Publication Date

2020-03-01

DOI

10.1029/2019jg005371

Peer reviewed

Correspondence to:
T. Treude,
ttreude@g.ucla.edu

Biogeochemical Consequences of Nonvertical Methane Transport in Sediment Offshore Northwestern Svalbard

T. Treude[1,2], S. Krause[3], L. Steinle[4], E. Burwicz[3], L. J. Hamdan[5], H. Niemann[4,6,7,8], T. Feseker[9], V. Liebetrau[3], S. Krastel[10], and C. Berndt[3]

[1]Department of Earth, Planetary and Space Sciences, University of California, Los Angeles, CA, USA, [2]Department of Atmospheric and Oceanic Sciences, University of California, Los Angeles, CA, USA, [3]GEOMAR Helmholtz Centre for Ocean Research Kiel, Kiel, Germany, [4]Department of Environmental Sciences, University of Basel, Basel, Switzerland, [5]School of Ocean Science and Engineering, University of Southern Mississippi, Ocean Springs, MS, USA, [6]Department of Marine Microbiology and Biogeochemistry, NIOZ Royal Netherlands Institute for Sea Research, and Utrecht University, Utrecht, The Netherlands, [7]Department of Earth Sciences, Faculty of Geosciences, Utrecht University, Utrecht, The Netherlands, [8]CAGE – Centre for Arctic Gas Hydrate, Environment and Climate, Department of Geosciences, UiT The Arctic University of Norway, Tromsø, Norway, [9]MARUM Center for Marine Environmental Sciences and Department of Geosciences, University of Bremen, Bremen, Germany, [10]Institute of Geosciences, University of Kiel, Kiel, Germany

Abstract A site at the gas hydrate stability limit was investigated offshore northwestern Svalbard to study methane transport in sediment. The site was characterized by chemosynthetic communities (sulfur bacteria mats, tubeworms) and gas venting. Sediments were sampled with in situ porewater collectors and by gravity coring followed by analyses of porewater constituents, sediment and carbonate geochemistry, and microbial activity, taxonomy, and lipid biomarkers. Sulfide and alkalinity concentrations showed concentration maxima in near-surface sediments at the bacterial mat and deeper maxima at the gas vent site. Sediments at the periphery of the chemosynthetic field were characterized by two sulfate-methane transition zones (SMTZs) at ~204 and 45 cm depth, where activity maxima of microbial anaerobic oxidation of methane (AOM) with sulfate were found. Amplicon sequencing and lipid biomarker indicate that AOM at the SMTZs was mediated by ANME-1 archaea. A 1D numerical transport reaction model suggests that the deeper SMTZ-1 formed on centennial scale by vertical advection of methane, while the shallower SMTZ-2 could only be reproduced by nonvertical methane injections starting on decadal scale. Model results were supported by age distribution of authigenic carbonates, showing youngest carbonates within SMTZ-2. We propose that nonvertical methane injection was induced by increasing blockage of vertical transport or formation of sediment fractures. Our study further suggests that the methanotrophic response to the nonvertical methane injection was commensurate with new methane supply. This finding provides new information about for the response time and efficiency of the benthic methane filter in environments with fluctuating methane transport.

1. Introduction

Marine methane has received major attention in the past three decades due to the concern that large methane reservoirs, locked up in the form of gas hydrates in continental margins (K. Kvenvolden, 1993; K. A. Kvenvolden, 1988), could be released into the atmosphere when unlocked by rising temperatures (Archer, 2007; Buffett & Archer, 2004; Krey et al., 2009; Nisbet, 1989). When added to the atmospheric inventory, methane acts as a potent greenhouse gas (Stocker et al., 2013). Current estimates of methane hydrate reservoirs vary (Boswell & Collett, 2011), but the most conservative calculations (4-995 Gt world-wide; (Burwicz et al., 2011; Wallmann et al., 2012)) are three orders of magnitude higher than annual global net methane emissions from natural and anthropogenic sources (500–850 Tg yr^{-1}; Kirschke et al., 2013), and give reasons to consider that if released into the atmosphere, methane from hydrate reservoirs could lead to an aggravated positive feedback on global warming. Calculations suggest a high probability for increasing temperatures in both the shallow and deep ocean (Stocker et al., 2013), presenting a scenario where release of methane from marine reservoirs seems possible. However, while the first projections of temperature-related methane releases from marine hydrates were rather drastic (Archer, 2007; Buffett &

Archer, 2004; Krey et al., 2009), later studies revealed that hydrate dissociation stemming from temperature rise is slow, possibly delayed by centuries or even millennia (Biastoch et al., 2011; Kretschmer et al., 2015; Ruppel, 2011), potentially providing enough time for methanotrophic microbes in sediment and in the water column to oxidize methane before catastrophic amounts enter the atmosphere (James et al., 2016; Knittel & Boetius, 2009). Still, continued discoveries of methane seeps along the gas hydrate stability zone (GHSZ) of continental margins around the world (Baumberger et al., 2018; Skarke et al., 2014; Westbrook et al., 2009) and the expectation of numerous more seeps yet to be discovered (Boetius & Wenzhöfer, 2013) place renewed importance on questions about potential releases of methane from the seafloor (Ruppel & Kessler, 2017).

The Arctic Ocean has received particular attention with respect to temperature-related hydrate dissociation for two reasons. One, the Arctic is experiencing the most dramatic temperature rise in the history of human-caused global warming (Stocker et al., 2013), and two, because arctic subseafloor hydrates are physically stable at shallower water depths (Hester & Brewer, 2009; Ruppel & Kessler, 2017; and references therein). That shallow stability makes Arctic hydrates more susceptible to atmospheric temperature increases and thus rises the likelihood of methane emissions reaching the atmosphere. Over the past decade, several field studies reported methane release from the shallow seafloor of the Arctic Ocean (e.g., Mau et al., 2017; Shakhova et al., 2014, 2010; Thornton et al., 2016; Veloso-Alarcón et al., 2019; Westbrook et al., 2009). Their sources, sinks, and potential connection to gas hydrate dissociation have been the focus of several follow-up studies and discussions (Berndt, Dumke, et al., 2014; Berndt, Feseker, et al., 2014; Graves et al., 2017, 2015; James et al., 2016; Myhre et al., 2016; Platt et al., 2018; Riedel et al., 2018; Ruppel & Kessler, 2017; H. Sahling et al., 2014; Steinle et al., 2015; M Torres & Colwell, 2018; Wallmann et al., 2018). Different models have also been applied to investigate past, current, and future methane releases from the Arctic seafloor (Biastoch et al., 2011; Crémière et al., 2016; Marín-Moreno et al., 2015, 2013; Reagan & Moridis, 2009; Thatcher et al., 2013).

An area of special research interest is the upper continental slope offshore western Svalbard. In 2008, Westbrook and coworkers discovered large areas of methane gas release along the GHSZ, raising the question if the released methane originated from dissociating gas hydrates (Westbrook et al., 2009). Since the discovery, two studies focused in particular on the causes of methane releases in the area. Berndt, Feseker, et al. (2014) postulated that the intensity of methane release could be seasonally driven due to the removal and formation of hydrates in surface sediment at temperature highs and lows, respectively, acting as an off/on barrier for rising methane. They further discovered that methane-derived authigenic carbonates in sediments along the water depth contour, where the base of the GHSZ intercepts with the seabed, date more than 3,000 years before present, thus substantially predating anthropogenic warming. However, since the collected carbonates provided no clues on changes in the release rate of methane from the seafloor, additional methane release caused by global warming cannot be excluded. In 2016, a drilling expedition in the area revealed porewater freshening of sediments related to gas hydrate dissociation (Wallmann et al., 2018). Numerical modeling suggest that the destabilization of the hydrates started around 8,000 years before present, which coincided with the time when isostatic uplift due to postglacial rebound outpaced eustatic sea-level rise, i.e., when hydrates became unstable due to depressurization. The study further concluded that the gas hydrates were not a major source of methane release from the seafloor at present but that their role to act as a seal for the release of deeper methane gas could be a more important control on methane seepage.

From a microbiological science perspective, one of the major questions that remain with regard to the fate of methane released from gas hydrates or liberated from deeper sources is the response time of the benthic methanotrophic community to efficiently control methane emissions. Biogeochemistry can provide important information on the history, dynamics, and pathways of methane transport through sediment. The major sink of methane in marine sediment is the microbial anaerobic oxidation of methane (AOM) coupled to sulfate reduction (Knittel & Boetius, 2009):

$$CH_4 + SO_4^{2-} \rightarrow HCO_3^- + HS^- + H_2O. \tag{1}$$
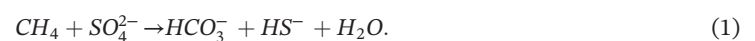
The simultaneous consumption of methane and sulfate by AOM creates a sulfate-methane transition zone (SMTZ), where sulfate diffusing into sediment from above overlaps with dissolved methane transported
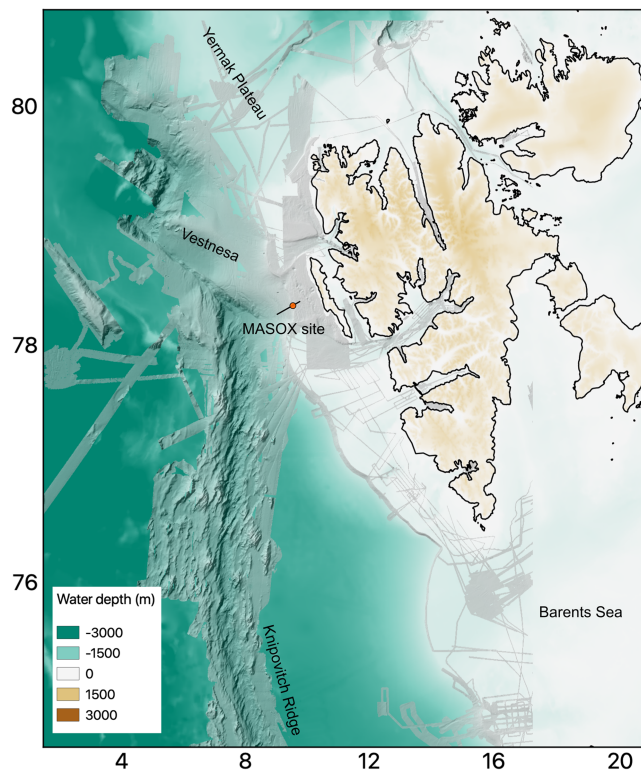
Figure 1. Map showing the study area (MASOX site) off Svalbard including multibeam bathymetry.

from below (Iversen & Jørgensen, 1985). In diffusive systems, sulfate and methane concentrations typically linearly decrease to their point of consumption (Jørgensen et al., 2001; Treude, Niggemann, et al., 2005). In advective systems with uprising fluid flow, sulfate and methane profiles show concave-down curvatures with positive and negative slopes, respectively, caused by sulfate-free, methane-rich pore fluid advecting faster against the sulfate-rich methane-free seawater diffusing down (Treude et al., 2003; Wallmann et al., 2012). With increasing upward fluid flux, the SMTZ is pushed closer to the sediment-water interface (Treude, 2003), to the point when the flux is so high that sulfate penetration into the sediment is prevented thereby excluding sulfate-dependent AOM and reducing biological control on emission (Niemann et al., 2006). When at steady state, the curvature of the sulfate profile is defined by the rate of fluid advection (Darcy's flow) and microbial sulfate reduction (Wallmann et al., 2012). When at nonsteady state, models fail to reproduce sulfate profiles when applying constant advection and sulfate reduction rates, indicating disequilibrium. Such information can be useful to identify changes in fluid flux and corresponding methane transport.

Here, we present new sediment data from a gravity core obtained within the GHSZ offshore western Svalbard showing nonsteady state methane flux, as manifested by two (deep and shallow) SMTZs. We use geophysical, geochemical, metabolic, and molecular data as well as a 1D modeling approach to interpret the age and formation mechanism of the SMTZs. In combination with data gained from in situ sediment porewater collectors (peepers) deployed in the nearby surface sediment, we hypothesize that the shallower SMTZ formed more recently as a result of nonvertical methane transport, induced by detouring of vertical methane transport. The purpose of this study was to provide new insights into the microbial controls of methane transport in sediments and the potential response time of the microbial community to a new methane supply.

2. Materials and Methods

2.1. Study Site

The outer shelf and upper continental slope of northwestern Svalbard (80–415 m water depth) are characterized by widespread occurrence of methane gas venting from the seafloor, with strongest intensity near the 400 m isobath, which overlaps with the GHSZ (Riedel et al., 2018; Sahling et al., 2008; Westbrook et al., 2009). Waters at this depth are dominated by the northward-flowing West Spitzbergen Current, which transports water from the North Atlantic to the Arctic Ocean. This water mass has experienced unprecedented temperatures in the early 21st century, which are presumably linked to the Arctic amplification of global warming (Spielhagen et al., 2011). Sources and migration pathways of gas and the distribution of gas hydrates in the area are debated due to complicated seismic interpretations. Detailed geophysical, sedimentological, and hydrographic summaries have been published elsewhere (Goswami et al., 2016; Graves et al., 2017; Ker et al., 2014; H. Sahling et al., 2014; Westbrook et al., 2009).

The study site is located at the 394 m isobath in 178 m distance from the Monitoring Arctic Seafloor-Ocean Exchange (MASOX) observatory (78°33.30 N, 09°28.61 E; Berndt, Feseker, et al., 2014, Figure 1), which was recovered during the same expedition (R/V Maria S. Merian expedition MSM21/4, 2012). Exact locations and water depths of sampling events of the present study are provided in Table 1. The MASOX area (394 m water depth) is at the upper limit of the GHSZ (~390 m; Riedel et al., 2018). The calculation of the limit is based on the summer month August, which coincides with the study period (late August/early September) (Riedel et al., 2018). Gas hydrate stability in the surface sediments at this water depth likely varies seasonally (Berndt, Feseker, et al., 2014; Ferré et al., 2020; Veloso-Alarcón et al., 2019) and moves the upper limit of the GHSZ between ~360 m during coldest (April to June) and ~410 m during warmest (November to

Table 1
MASOX Station Sampling Protocol

Date	MSM21-4 Station no.	Latitude (N)	Longitude (E)	Water depth (m)[a]	Sampling instrument	Temparature at seafloor (°C)[b]	Activity/samples
23.08.2012	578-1	78°33.343	09°28.416	394	JAGO	3.84	Peeper and heat flow probe deployment
23.08.2012	579-1	78°33.344	09°28.414	394	JAGO	3.81	Carbonate sampling from sediment surface
02.09.2012	647-1	78°33.344	09°28.404	393	JAGO	3.66	Peeper and heat flow probe retrieval
04.09.2012	657-1	78°33.34	09°28.38	388	Gravity Corer	n.d.	Sediment core sampling, rope length 393 m

[a]Water depth determined by either JAGO (peeper, carbonates) or R/V meteor (gravity corer).   [b]Average temperature at the seafloor during JAGO operations at the peeper site.

March) conditions at the seafloor. Aside from seasonal temperature variability, rapid temperature changes associated with current-driven hydrography occur. For example, during the study, temperatures at the seafloor changed from colder (~3.2°C) to warmer (>4°C) due to meandering of the West Svalbard Current (Steinle et al., 2015); i.e., the bottom water is colder when the current is located further offshore opposite to when it has a position closer to the coast.

2.2. Geophysical Measurements

During the R/V Maria S. Merian MSM21/4 expedition, seismic equipment was used to acquire a dense net of high-resolution multichannel seismic data covering the west Svalbard margin from the shelf to the oceanic crust (Berndt et al., 2014). The system consisted of a 1.7l GI-Gun in harmonic mode, which was towed at 0.7 m depth and triggered every 6 and 7 s intervals for shallow and deep-water depth, respectively. The data were collected with a 225-m-long digital streamer with 144 channels. The data were filtered, binned at 6.25 m, stacked, and time migrated with water velocity (Stolt migration). The final horizontal and vertical resolution within the surface sediments is about 6–7 m. Our data were complemented with those collected in 2008 during the James Clark Ross cruise 211. These were acquired with the same source but with a 600-m long streamer. The data were processed using prestack depth migration (see Sarkar et al., 2012 for processing details).

To image the shallow subsurface (<50 m) and gas flares in the water column, a hull-mounted parametric subbottom profiler PARASOUND DS3 (Atlas Hydrographic) was run continuously to obtain a dense grid of shallow subsurface data around the MASOX site (Berndt et al., 2014). PARASOUND DS3 works as a narrow beam sediment echo sounder, providing primary frequencies of 18.5–28 kHz (primary high frequency), generating parametric secondary low frequencies ranging 0.5–10 kHz and secondary high frequencies 36.5–48 kHz, respectively. Secondary frequencies are caused by nonlinear acoustic interaction of the primary waves at high signal amplitudes. The emission cone of the high-frequency primary signals has an aperture angle of 4° for the PARASOUND DS3. The narrow aperture is achieved using an array of 128 transducer array on an ~1 m^2 rectangular plate. The footprint is 7% of the water depth.

2.3. In Situ Porewater Sampling Using Peepers

Peeper systems for in situ porewater sampling were built after Dattagupta et al. (2007) with several modifications (see details below) and are based on equilibration of chemical solutes, contained within a fluid cell, with the surrounding medium across a dialysis membrane. The inner peeper tube consisted of a polyoxymethylene rod (1.6 cm diameter, 51 cm length) with eight chambers (1 cm W × 1.5 cm D × 4 cm H cm) for dialysis bags. Each chamber collected porewater over a distance of 4 cm sediment depth. The back of the chambers (1 × 4 cm area) was perforated with small holes (1 mm diameter) to permit solute exchange between chambers and surrounding environment once deployed. The total distance between individual chambers was 1 cm. The distance from the topmost to the bottom most chamber was 39 cm: 8 chambers × 4 cm height + 7 × 1 cm distance. If fully inserted into sediment, the window of the topmost chamber started at 2 cm below seafloor (cmbsf). Dialysis tubing (cellulose ester dialysis membrane, 10 mm diameter, MWCO: 1,000,000, Spectrum Labs, Inc.) was filled with 0.2 µm filtered (operationally sterile) seawater. Seawater was collected in the sampling area by CTD/Rosette at 340 m. Both ends of the tubing were closed with small cable ties to form cylindrical bags, which were fitted into the peeper chambers. After the bags were placed into the chambers, an outer titanium liner (1.6 cm i.d., 1.9 cm o.d., and 51 cm length)
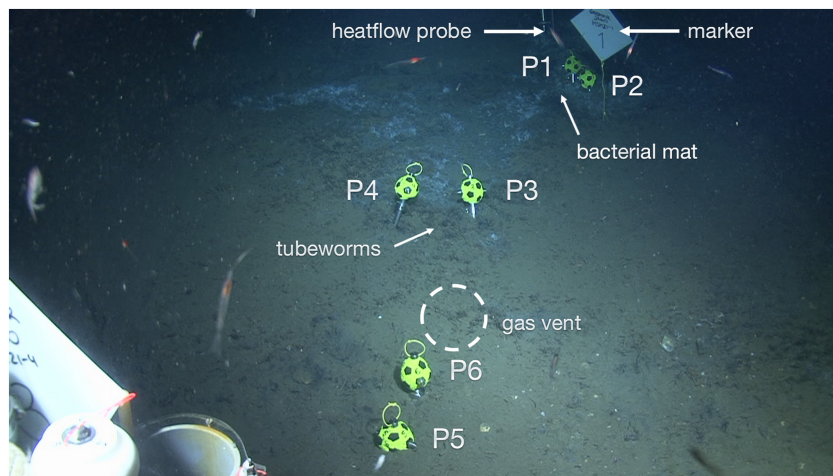
Figure 2. Benthic deployment of six peepers (P1–P6), the heat flow probe, and a marker at the MASOX station (394 m) achieved by the submersible JAGO. P1/P2 and the heat flow probe were deployed within a bacterial mat, P3/P4 within a tubeworm field, and P5/P6 close to a gas vent. For more details, see text and Figure S1. As a reference, the size of Marker 1 was 20 × 20 cm.

covered the inner polyoxymethylene tube. The liner had eight windows the same size as the inner tube chambers, positioned exactly over the perforated chamber backside to enable solute exchange. The chambers were filled completely with sterile seawater and the windows were sealed with parafilm to prevent evaporation of water until deployment. Parafilm was removed, and peepers were deployed by the submersible JAGO (for station details, see Table 1).

The selected sampling site was located within the MASOX station area and consisted of an inner sediment patch covered by sulfur bacteria and siboglinid tubeworms, surrounded by an outer margin of siboglinid tubeworms without visible sulfur bacteria (Figures 2 and S1). Within the inner patch, filamentous sulfur bacteria covered tubes, sediment, and rocks. At one end of the patch, outside the outer margin, gas bubble venting was observed (Figure S1). The total sampling area was approximately 4 m in length and 1.5 m in width. Replicate peepers were placed within the bacterial mat area (Peepers 1 and 2), the tubeworm field (Peepers 3 and 4), and close to the gas venting (Peepers 5 and 6) (for exact positions of peepers, see Figures 2 and S1). The distance between peeper sites was approximately 1 m. Due to the presence of cobbles and carbonates, peeper penetration depth differed. The approximate depth of the first chamber was noted to reconstruct the relative depth of all chambers. All peeper chambers were completely pushed into the sediment, except for the topmost chamber of Peeper 4 (Figures 2 and S1), which was situated at the sediment-water interface and therefore sampled a mixture of both sediment porewater and overlying bottom water. Furthermore, the window of this chamber was in proximity to small protruding tubeworm bushes, which complicated interpretation, as tubeworms facilitate mixing between pore fluids and seawater (Cordes et al., 2005). Peepers were deployed for 10 days, during which solute concentrations in the dialysis bags equilibrated with those of the sediment porewater. After retrieval, dialysis bags were removed from chambers; water was subsampled with needle syringes and immediately processed for geochemical analyses (see below).

2.4. Temperature Measurements

In situ bottom water temperature at the peeper site was recorded during sampling using a CTD system mounted to JAGO's stern. The system continuously recorded conductivity, temperature, and depth at intervals of 10 s.

In situ sediment temperature at the peeper site was profiled using a short (40 cm length) temperature probe (Feseker et al., 2012), deployed by JAGO within the bacterial mat, approximately 1 m from Peepers 1 and 2, 2 m away from Peepers 3 and 4, and 3 m away from Peepers 5 and 6 (Figures 2 and S1, Table 1). The instrument consisted of eight temperature sensors placed 4.5 cm apart, resulting in an active length of 31.5 cm. The sensor string was connected to a data logger mounted directly to the lance. The sensors were calibrated to a precision of ± 1 mK prior to the deployment. The temperature probe was inserted vertically into the sediment

by JAGO until all sensors were buried. Temperature readings were recorded every 10 s for the duration (~10 days) of the peeper deployment.

2.5. Surface Carbonate Sampling

Carbonates were scooped from the top 10 cm of sediments at the peeper station using JAGO push cores (6 cm diameter, 25 cm length; for station details, see Table 1). Proper sediment coring was not possible with push cores due to the presence of carbonates and cobbles. On board, push cores were emptied into trays, sediment was removed, and carbonates were wrapped in aluminum foil and stored at +4°C until analysis.

2.6. Sediment Sampling

Following completion of JAGO operations, a gravity corer equipped with a 6-m long steel barrel (inner diameter 13 cm) and a 2-t weight was used to collect sediment. The steel barrel was lined with a plastic bag (diameter 12.7 cm) that contained the sediment core. During coring operation, the ship's instrument deployment center was positioned and maintained directly above the peeper station using dynamic positioning. The gravity corer was deployed ~7 m west of the peeper station (Table 1). Given the shallow water depth and minimal wire angle, the core was likely representative of the JAGO operations area; however, without acoustic positioning gear mounted on the gravity corer, some uncertainty (a few meters) in core positioning might have occurred. After retrieval, the core catcher was removed, and the plastic bag liner was transferred to a core table and cut open lengthwise. The total core recovery was 210 cm and consisted of dark-gray clay and silt. Tubes of sibuglinid tubeworms were detected in the top ~10 cm of the core. Between the top and 54 cmbsf, sediment was foamy (from degassing) and crunchy (from carbonate pellets). Gas bubbles were detected in the sediment at 42–43 cmbsf. Below 54 cmbsf, the sediment was soft without indications of degassing or abundance of carbonate pellets. The core had a strong sulfidic smell.

In total, 12 sediment layers equally distributed down core (18 cm intervals), plus the core catcher, were subsampled for different analyses. Immediately after retrieval, 2 cm^3 sediment plugs were taken for methane (CH_4) analyses with a 2.5-ml cutoff syringe, transferred to a 10-ml serum glass vial filled with 5 ml 2.5% sodium hydroxide solution, crimp-sealed with butyl stopper and aluminum crimp, shaken thoroughly, and stored at +4°C. Three replicate samples each for the determination of sulfate reduction and AOM, respectively, were taken with glass tubes equipped with a syringe plunger and sealed with a thick butyl stopper according to (Treude, Krüger, et al., 2005). Additional sediment was collected for control samples. Approximately 3-cm thick layers were cut from the core, wrapped in parafilm (Pechiney Plastic Packaging) and transferred to a cold room (+4°C) for pore water extraction (Section 2.7). Eight milliliter of sediment was taken with a cutoff 10 ml syringe, transferred to preweighted plastic vials, and stored at +4°C for porosity, density, and elemental (C and N) analyses. Approximately 50 g of sediment was wrapped in aluminum foil and frozen at −20°C for biomarker analyses. Approximately 4 ml of sediment was sampled into cryovials and frozen at −80°C for molecular analyses. Carbonate samples (nodules 1–5 cm in size) were combined from different depth sections (0–60, 60–120, and 120–210 cmbsf) to collect sufficient material for analysis, wrapped in aluminum foil and stored at +4°C. Carbonates collected at the bottom of the core (210 cm) were cemented around snail shells (likely *Colus* sp. of the carnivorous/scavenging family *Buccinidae*, L. Levin, pers. comm.), which might have prevented a deeper penetration of the gravity corer into sediment.

2.7. Porewater Extraction

Porewater was extracted onboard using a low-pressure squeezer (argon at 1–5 bar) at +4°C inside a cooled laboratory container. While squeezing, porewater was filtered through 0.2 μm cellulose acetate nuclepore filters and collected in argon-flushed recipient vessels. Onboard, the collected porewater samples were analyzed for their content of dissolved total sulfides (in the following referred to as "sulfide"), ammonium (NH_4^+), and total alkalinity, whereas analyses of chloride (Cl^-), sulfate (SO_4^{2-}), and the oxygen isotopic composition of water ($\delta^{18}O$) were performed onshore. These porewater samples were stored in 2-ml glass vials at +4°C.

2.8. Porewater Analyses

Sulfide and ammonium were determined using standard photometric procedures. Sulfide measurements were modified after (Cline, 1969). A 1 ml sample was added to 50 µl of zinc acetate solution. Subsequently, 10 µl of N,N-dimethyl-1,4-phenylenediamine-dihydrochloride color reagent solution and 10 µl of the $FeCl_3$ catalyst were added and mixed. After 1 hr of reaction time, the absorbance was measured at 670 nm. The concentration of ammonium was measured after Grasshoff et al. (1999). A 1 ml sample was diluted 5 times with ultrapurified water, followed by addition of 200 µl phenol solution. Subsequently, 100 µl of citrate buffer and 200 µl of the dichloro-s-triazine-2,4,6-(1H,3H,5H)-trione sodium reagent solution were added. After mixing, samples were kept in the dark at +40°C for 1 hr before absorbance measurements (630 nm). Total alkalinity was determined by direct open-cell titration in a titration vessel after Bruevich (Bruevich, 1944; Pavlova et al., 2008). For measurements the vessel was continuously flushed with argon through the liquid to strip and remove forming CO_2 and H_2S during acidification. Initially, 20 µl of a methyl red/methylene blue color reagent was added, followed by 1 ml of sample. Titration was carried out using 0.01 M HCl until color change occurred. For calibration, IAPSO standard seawater was used with a precision and detection limit of 0.05 mEq L^{-1}. Chloride and sulfate were determined by ion chromatography (Methrom, IC Compact 761). Analytical precision based on repeated analysis of IAPSO standards (dilution series) was <1%. $\delta^{18}O$ of porewaters was analyzed with an off-axis integrated-cavity-output spectroscope (LWIA-24-EP, Los Gatos Research, USA). The instrument was calibrated using the international water isotope standards VSMOW2, GISP, and SLAP2, and precision was monitored by measuring each sample 7 times.

2.9. Sediment Parameters

Sediment porosity was determined gravimetrically by calculating the difference between the wet and dry weight of the sediment sample divided by its volume (8 ml). For the determination of the sediment dry weight, samples were freeze-dried. Sediment density was determined by dividing wet weight of the sediment sample by its volume (8 ml). Wet sediment samples for analysis of particulate organic carbon (POC) and particulate organic nitrogen were freeze-dried and analyzed using a Carlo-Erba element analyzer (NA 1500). POC content was determined after acidification with HCl (0.25 N) to release the inorganic components as CO_2. Weight percent of total carbon was determined without acidification. Inorganic carbon was determined by weight difference between total carbon and organic carbon. The precision and detection limit of the POC analysis was 0.04 and 0.05 dry weight percent (% C), respectively. Precision and detection limit of the inorganic carbon analysis was 2 and 0.1% C, respectively.

2.10. Methane Analyses

Methane was determined onshore by gas chromatography in the headspace of the crimp-sealed glass vials from 100 µl aliquots, subsampled with a gas-tight microliter syringe. The gas chromatograph (Shimadzu, GC-2014) was equipped with a packed Haysep-D column (Shimadzu) and a flame ionization detector. The column temperature was +80°C and the helium flow was set to 12 ml min^{-1}. Methane concentrations were calibrated against methane standards. The detection limit was 0.1 ppm with a precision of 2%.

2.11. Determination of AOM and Sulfate Reduction Activity With Radiotracers

[14]C-methane dissolved in seawater (injection volume 15 µl, activity 5 kBq, specific activity 2.28 GBq $mmol^{-1}$) was injected into each sample through the rubber stopper. Samples were incubated shipboard at in situ temperature (3°C) for 24 hr in the dark. To terminate microbial activity, samples were transferred to 40-ml glass vials filled with 20-ml sodium hydroxide (2.5% w/w) and closed immediately with rubber stoppers. The vials were shaken to equilibrate porewater methane between aqueous and gaseous phase. In the home laboratory, AOM rates were determined according to Treude, Krüger, et al. (2005) (gas chromatography, ^{14}C-methane combustion, and calculation) and Joye et al. (2004) (^{14}C-CO_2 trapping).

Injection and incubation procedures for sulfate reduction were similar as for AOM. To each sample, 6 µl of carrier-free ^{35}S-sulfate (activity 200 kBq, specific activity 37 TBq $mmol^{-1}$) was injected. Microbial activity was terminated by transferring samples into 50-ml plastic centrifuge tubes containing 20 ml of zinc acetate (20% w/w) and freezing at −20°C. Samples were kept frozen until further analysis. Rates were determined using the cold-chromium-distillation method (Kallmeyer et al., 2004).

AOM and sulfate reduction rates were corrected for (insubstantial) tracer turnover in killed controls. Killed controls for AOM and sulfate reduction were terminated with sodium hydroxide and zinc acetate, respectively, before tracer addition. We conservatively only considered $_{14}$C and $_{35}$S tracer turnover as biological if the recorded turnover was higher than the mean turnover plus three times the standard deviation of the killed controls.

2.12. Biomarker Analyses

For lipid biomarker analyses, ~50 g of sediment per depth layer was sampled with a metal spatula, wrapped in aluminum foil and stored at −80°C until extraction in the home laboratory. An aliquot of 20 g of sediment was spiked with 100 μl of internal standard (50 ng μl^{-1} of the fatty acid n-C:19:0, the alcohol n-C19:0, and the hydrocarbons n-C36:0 and α-cholestane), extracted, and separated according to Elvert et al. (2003) and Niemann et al. (2005). Briefly, total lipid extract was obtained by ultrasonicating samples with solvents of decreasing polarity: (1) dichloromethane:methanol 1:2; (2) dichloromethane:methanol 2:1; and (3, 4) dichloromethane. Total lipid extract was separated into a polar fatty acid, hydrocarbon, keto, and alcohol fractions. The alcohol and polar acid fractions were derivatized into trimethylsilyl ethers with bis(trimethyl-silyl)trifluor-acetamide and into polar fatty acid methyl esters with methanolic BF$_3$, respectively. Double-bond positions of monoenoic polar fatty acids were determined through analysis of their dimethyl disulfide adducts (Moss & Lambert-Fair, 1989; Nichols et al., 1986).

Identities, concentrations, and stable carbon isotope composition of individual compounds were determined with a gas chromatograph linked to a quadrupole mass spectrometer, flame-ionization detector, or an isotope ratio mass spectrometer, respectively, as described in Steinle et al. (2018). Concentrations were calculated using the internal standard. Concentrations and the corresponding δ^{13}C values were corrected for the introduction of carbon atoms during derivatization (Niemann et al., 2005). The analytical error associated with measurements of concentrations and δ^{13}C values of baseline-separated individual compounds was ±10% and ±1‰, respectively.

2.13. Molecular Analyses

Genomic DNA was extracted using a modified FastDNA™ protocol described in detail by Hamdan et al. (2013) and Hamdan et al. (2018). DNA was quantified on a Qubit 2.0 Fluorometric Quantitation system (Invitrogen), and purity was determined by NanoDrop (ThermoFisher). The V6–V8 variable regions of the 16S rRNA gene were amplified using the primers B969F/BA1406R and A956F/A1401R for bacteria and archaea, respectively. Amplification and sequencing were performed according to protocols in Comeau et al. (2011) at the Microbiome Resource (IMR) facility at Dalhousie University. Approximately 50,000 sequences per sample were generated on an Illumina MiSeq. Raw partial 16S rRNA sequences were analyzed with the pipeline described in Salerno et al. (2018) that was created with the software packages USEARCH (v8.1) and UPARSE (Edgar, 2013) and Quantitative Insights into Microbial Ecology (QIIME, MacQIIME version 1.9.1) (Caporaso et al., 2010). UPARSE merged paired-end sequences, with minimum merge length of 200 base pairs (bps) and maximum difference in the overlap region allowing for a 20% error rate. Merged sequences were quality filtered based on Phred scores, and dereplicated unique sequences were used as the basis for operational taxonomic unit (OTU) assignment using greedy clustering at ≥97% similarity. Chimeric sequences were removed, and singletons were retained. An OTU relative abundance table was used for taxonomic identification and alignment to the GreenGenes reference database (v13.8). OTUs with taxonomic identification are subsequently describe herein as "phylotypes." Diversity statistics were calculated in QIIME.

2.14. Carbonate Analyses
2.14.1. XRD Analysis
For X-ray diffraction (XRD) measurements, powdered samples were obtained using a handheld drill (Proxxon FBS 240/E) with a 0.8 mm diameter ball-shaped diamond bit in low speed mode to avoid heating-induced alteration. The collected powder was additionally ground in an agate mortar and spread evenly onto a silicone mono-crystal disk. Subsequent XRD measurements were carried out between 2° and 70° 2-theta using a Philips X-ray diffractometer PW 1710 with monochromatic Co cathode. The spectrum analysis was done using the software package X-Powder (Version 2010.0134 PRO).

2.14.2. Carbonates $\delta^{13}C$ and $\delta^{18}O$ Analysis

From each homogenized carbonate powder sample (Section 2.14.1), an aliquot of 10 mg was separated for carbon $\delta^{13}C$ and oxygen $\delta^{18}O$ stable isotope analysis. A fraction of this powder (~1 mg) was dissolved in water-free phosphoric acid at +73°C in a "Carbo-Kiel" (Thermo Fischer Scientific Inc.) online carbonate preparation line and measured for carbon and oxygen stable isotope ratios with a MAT 253 mass spectrometer (Thermo Fischer Inc.). The $\delta^{13}C$ and $\delta^{18}O$ values are reported as ‰ deviations from the GEOMAR laboratory standard (Solnhofen limestone) referred to the V-PDB scale. Reproducibility was ±0.02‰ for $\delta^{13}C$ and $\delta^{18}O$ (1 SD).

2.14.3. U-Series Chronology

This study used U–Th age data from small samples (5.5–55.5 mg aliquots of the XRD and light stable isotope samples) to combine high lateral subsampling with the analytical precision of multicollector-inductively coupled plasma-mass spectrometry (MC-ICP-MS). The U–Th isotope measurements were performed on a VG Elemental AXIOM MC-ICP-MS at GEOMAR applying the multistatic multi-ion-counting (MIC)-ICP-MS approach after (Fietzke et al., 2005). For isotope dilution measurements, a combined $^{233/236}U/^{229}Th$ spike was used, with stock solutions calibrated for concentration using NIST-SRM3164 (U) and NIST-SRM3159 (Th) as combi-spike calibrated against CRM-145 uranium standard solution (also known as NBL-112A) for U-isotope composition and against a secular equilibrium standard (HU-1, uranium ore solution) for determination of $^{230}Th/^{234}U$ activity ratio. Whole procedure blank values of this sample set were measured around 0.1 fg (±50%, 2 SD) for ^{230}Th, around 7 pg for ^{232}Th (±30%, 2 SD) and between 3 and 10 pg for U, which are in the typical range of this method and laboratory. The Eichrom-UTEVA resin was used for U and Th separation. Calculation of geochronological data and activity ratios is based on the decay constants given by Cheng et al. (2000).

From all original samples, powder aliquots were attacked by 4 N acetic acid in order to provide weak leachates mainly dissolving the carbonate phase. Accepting by purpose the theoretical risk of fractionating U and Th due to the higher particle reactivity of the latter and potential relative loss of ^{230}Th when compared to the parent isotope ^{234}U, these weak leachates provide minimum values in the direct $^{230}Th/^{234}U$ age determination. Where available, an additional powder aliquot of the original sample (marked by sample code suffix-2, Table 2) was attacked by 2.25 N HNO_3 to provide a stronger leachate and potentially significant isochron spread.

Each set of element separation was accompanied by runs of aliquots of the HU-1 equilibrium standard solution to ascertain that the procedure is reproducible. A methodology-dependent uncertainty of less than 0.5% (2 SD) on $^{230}Th/^{234}U$ activity ratios was reached. The geochronological uncertainties presented here are dominated by the analytical error of individual sample measurements and the uncertainty of correction factors. An applied data reduction included a correction for isotopic composition of incorporated Th of detrital origin, according to average continental crust values (Wedepohl, 1995) as approximation for involved shelf sediments (Table 2). For the majority of samples, this correction is almost negligible, but some samples were dominated or even overcompensated to negative $^{230}Th/^{234}U$ activity ratios, due to low $^{230}Th/^{232}Th$ activity ratios and high Th concentrations. The sample selection strategy of our study is optimized for direct age determination of single phases of predominately aragonitic composition as discussed in Liebetrau et al. (2010). The Rosholt and Osmond isochron approaches presented here are based on the isoplot 3.75 software of the Berkeley Geochronology Center (CA, USA) and provide age estimates from 2-point reference lines. The $^{234}U/^{238}U$ ratios are presented in $\delta^{234}U$ notation.

2.15. Numerical Model

In this study, a 1D transport-reaction model based on the framework from Burwicz and Rüpke (2019) and Burwicz et al. (2011) with a fixed mesh size ($z_0 = 0$ m, $z_{max} = 2.5$ m) was used. Model formulation included solid sediment grains of a constant density (see Table 3 for specific parameter values), pore fluids fully saturating sediment porosity, a solid POC fraction available for biodegradation, and dissolved chemical species (methane, sulfate, and dissolved inorganic carbon [DIC]). Mass balance for solid species is constituted by the Equation 2:

Table 2
U–Th Geochronology and $\delta^{13}C$ of Carbonate-enriched Sediments at MASOX Site

MSM-21/4 stat. device and sediment depth (cmbsf)	Sample code and leachate mode[a]	Description	Repres. nonsilic. fract. (%)[b]	Age (kys BP)[c]	(^{230}Th/^{232}Th)	$\delta^{13}C$ (V-PDB)
579-1 Jago (0–10)	SV-28 (weak)	Concretionary dark matrix	24	3.4 ± 0.3	3.54 ± 0.03	−31.95 ± 0.01
579-1 Jago (0–10)	SV-29 (weak)	Carbonate domin. concret.	67	5.0 ± 1.1	2.21 ± 0.02	−36.52 ± 0.01
	28 and 29[d]			*2.5 ± 0.1*		
	28 and 29[e]			*2.8 ± 0.1*		
657-1 GC (40–50)	SV-20-1 (weak)	Less unconsolidated sed.	6	*0.6 ± 0.9*	1.13 ± 0.02	−27.12 ± 0.02
657-1 GC (40–50)	SV-20-2 (strong)	Less unconsolidated sed.	13	*0.5 ± 33.7*	0.80 ± 0.01	
657-1 GC (40–50)	SV-21 (weak)	Solidified sedim.	55	6.6 ± 0.4	4.72 ± 0.04	−41.34 ± 0.02
	20-1 and -2[d]			*0.55 ± 0.04*		
	20-1 and -2[e]			*0.62 ± 0.04*		
657-1 GC (60–120)	SV-22-1 (weak)	Less unconsolidated sed.	29	13.0 ± 5.0	1.72 ± 0.01	−36.37 ± 0.01
657-1 GC (60–120)	SV-22-2 (strong)	Less unconsolidated sed.	29	*−1.9 ± 64.1*	0.71 ± 0.01	
657-1 GC (60–120)	SV-23-1 (weak)	Solidified sedim.	43	11.9 ± 2.6	2.22 ± 0.02	−38.07 ± 0.03
657-1 GC (60–120)	SV-23-2 (strong)	Solidified sedim.	45	*0.3 ± 98.8*	0.76 ± 0.01	
	22-1 and -2[d]			*18.0 ± 0.3*		
	22-1 and -2[e]			*21.7 ± 0.4*		
	23-1 and -2[d]			*16.3 ± 0.2*		
	23-1 and -2[e]			*19.44 ± 0.4*		
657-1 GC (120–210)	SV-24-1 (weak)	Less unconsolidated sed.	18	22.9 ± 17.2	1.40 ± 0.01	−39.16 ± 0.03
657-1 GC (120–210)	SV-24-2 (strong)	Less unconsolidated sed.	22	*−15.1 ± 188.9*	0.62 ± 0.01	
657-1 GC (120–210)	SV-26 (weak)	Solid filling of gastropode	50	18.8 ± 13.3	1.41 ± 0.01	−41.11 ± 0.01

Note. Round brackets denote activity ratio. Uncertainties presented on 2 sigma level. Extracted from and modified after Berndt et al. (2014).
[a]For subsamples postulated of cogenetic origin by petrographic observations the isoplot 3.75 software of the Berkeley Geochronology Center, CA, USA is applied for isochron age estimates. [b]The equivalent percentage of the analyzed nonsilicate fraction represented by the sample weight. X-ray diffraction analyses indicated aragonite as the main nonsilicate and easily dissolvable phase. [c]Italics mark highly unreliable ages characterized by uncertainties larger than the deduced age or even dominated by ^{230}Th correction values as well as isochron approaches based just on 2-point reference lines. Therefore, the latter may not provide any proof for the petrographic postulation of cogenetic origin. [d]Age estimates applying the Rosholt-1 isochron approach in three-dimensional projection according data reduction system after Ludwig (2008). [e]Age estimates applying the Osmond isochron approach according data reduction system after Ludwig (2008).

$$(1-\phi)\frac{\partial G}{\partial t} = -\frac{\partial((1-\phi)v_s G)}{\partial z} + (1-\phi)R, \tag{2}$$

where φ is porosity, G denotes concentration of solid species (wt. %), t is time (s), z is depth (m), v_s is the burial velocity of sediments (m s^{-1}), and R denotes reaction rates.

Mass balance for dissolved compounds follows Equation 3:

$$\phi\frac{\partial C}{\partial t} = -\frac{\partial(\phi v_f C)}{\partial z} + \frac{\partial\left(\phi D_s\frac{\partial C}{\partial z}\right)}{\partial z} + \phi R, \tag{3}$$

where C is concentration of dissolved species (mM), v_f is Darcy's velocity of fluid (m s^{-1}), and D_s is the diffusion coefficient (m s^{-1}).

A constant geothermal gradient was calculated from bottom water temperature value reported for the study site (at the moment of sampling), bulk thermal sediment conductivity, and heat flow (see Table 3 for details) according to the Equation 4.

$$T_z = T_{BWT} + q/\lambda_b, \tag{4}$$

where T is temperature (°C), T_{BWT} denotes bottom water temperature (°C), q is heat flow at the lower boundary, and λ_b is the bulk thermal conductivity of sediments (W m^{-1} K^{-1}).

Pore fluid pressure was set to hydrostatic pressure at the beginning of the simulation. Afterwards, numerical finite element scheme was used to calculate pore fluid pressure following the solution from Schmidt et al. (2018). Pore fluid transport was simulated as Darcy flow (Equation 5), whereas sediment velocity was calculated according to Equation 6.

Table 3
Values of Parameters Used in the Numerical Study

Parameter	Symbol	Value	Unit	Equation	Reference
Number of nodes in z- direction	nnod	100	-	-	This study
Seafloor coordinate	z_0	0	m	-	This study
Max. depth	z_{max}	2.5	m		This study
Time-step	dt	50	years	-	This study
Total simulated time	t_{max}	5,500	years	-	This study
Sediment grain density	ρ_s	2,650	kg m^{-3}	-	Hantschel and Kauerauf (2009)
Pore fluid density	ρ_f	1025	kg m^{-3}	-	-
Seafloor porosity	φ_o	0.5489	-	-	Data fitting
Porosity at z_{max}	φ_{max}	0.4730	-	-	Data fitting
Heat flow	hf	0.05	W m^{-2}	-	This study
Water depth	wd	394	m	-	This study
Salinity	S	35	PSU	-	This study
Bottom water temperature	T_{BWT}	3.01757	°C	-	Data fitting
Temperature	T_z	-	°C	Equation (4)	-
Bulk thermal sediment conductivity	λ_b	2.2	W m^{-1} K^{-1}	-	
Pore fluid viscosity	υ_f	10^{-4}	Pa s	-	
Sediment tortuosity	To	2.1358–2.6020	-	$1 - 2 \log(\varphi)$	Calculated here
Permeability	k	-	-	$0.5 \, (\varphi^3)./(To^2)*(10^7)^2$	Calculated here
CH$_4$ upper boundary concentration	CH$_{4ini}$	0.00263	mM	-	This study
SO$_4$ upper boundary concentration	SO$_{4ini}$	28.5	mM	-	This study
DIC upper boundary concentration	DIC$_{ini}$	1	mM	-	This study
POC upper boundary concentration	POC$_{ini}$	0.85	wt.%	-	This study
Sedimentation rate	υ_0	5×10^{-4}	m year^{-1}	-	For details, see Section 2.
Burial sediment velocity	υ_s	-	m s^{-1}	Equation (6)	-
Darcy's fluid flow	υ_f	-	m s^{-1}	Equation (5)	-
Initial time for POC degradation	a_0	4,000	years	-	This study
Monod inhibition constant of POC degradation	Kc	1	mM	-	Wallmann et al. (2006)
Inhibition constant of CH4 formation by SO4	K_{SO4}	1	mM	-	Wallmann et al. (2006)
Kinetic constant of AOM (SMTZ-2)	k_{AOM}	1.5×10^{-1}	dm^3/(mmol year^{-1})	-	This study
Kinetic constant of AOM (SMTZ-1)	k_{AOM}	2		-	This study

$$\upsilon_f = -k/\mu_f(\partial P/\partial z - \rho_f g), \tag{5}$$

where k is permeability, μ_f is fluid viscosity (Pa s), P is pore fluid pressure (Pa), ρ_f denotes fluid density (kg m^{-3}), and g is gravitational acceleration (Pa m^{-2} kg^{-1}).

$$\upsilon_s = \upsilon_0(1 = \varphi_0)/(1 - \varphi), \tag{6}$$

where υ_s is solid grain velocity (m s^{-1}), υ_0 is sedimentation rate (m s^{-1}), and φ_o is seafloor porosity.

Additionally, transport of chemical species was modeled assuming diffusion according to molecular and sediment diffusion coefficients calculated separately for each species. Upper boundary conditions for chemical species concentrations were fixed throughout the simulation with values reported in Table 3. Chemical reaction of AOM, sulfate reduction, in situ POC degradation, and methanogenesis followed formulations from Burwicz et al. (2011). A substepping method was used to stabilize the code at the reaction front where gradients were highest. Depending on the chemical reaction rates at each time step, the main time-stepping loop was divided into smaller substepping routines in the chemical reaction solver. Thus, the overall time of the simulation was undisturbed, and the mass of all components was conserved. Crucial parameters (see Table 3 for details and values) for fitting the geochemical profiles to the measured data were related to AOM specifically and expressed by the Monod inhibition constant (K_c), kinetic constants for AOM (k_{AOM}; note different values for two separate SMTZs), and the inhibition constant of methane formation by sulfate (K_{SO4}). In our simulations, a constant K_c parameter with a value of 1 mM and a constant K_{SO4} parameter (1 mM) following the approach of Graves et al. (2017) was used. Moreover, we assume that total alkalinity was controlled by the carbonate system and reflected DIC concentrations. The upper boundary concentration of DIC (1 mM) which represents the mean seawater value was used in the model. Unlike to the
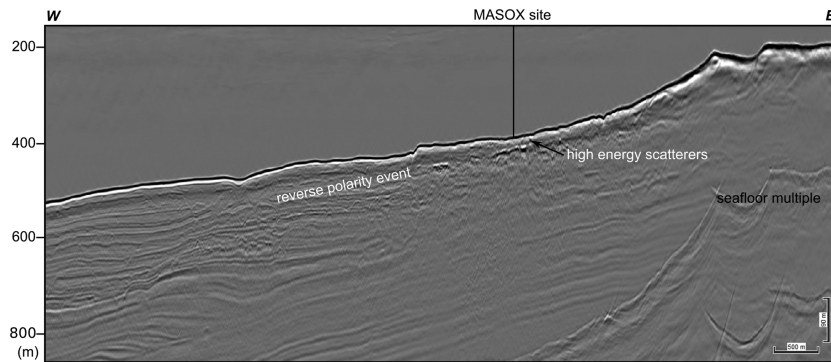
Figure 3. Prestack depth migrated line JR211-03 (after Sarkar et al., 2012) showing reverse polarity at shallow depth indicating the presence of free gas. The MASOX site is at the transition from glacigenic diamictons in the east to a contouritic glacimarine sedimentation in the west.

approach from Graves et al. (2017), the model used measured sediment porosity as an input. As a result, sediment porosity distribution affects solid velocity of sediments (see Equation 6) and, consequently, the burial rate of POC, which leads to differences in organic matter distribution with depth.

Laterally, the sedimentation rate v_0 on the Svalbard margin is highly variable as bottom currents lead to winnowing in some areas and redeposition in others. Furthermore, a general increase in sedimentation rate toward the shelf may be expected. In the absence of better constraints, we used a sedimentation rate of 50 cm kyr^{-1} which is 2–3 times higher than the 8–20 cm kyr^{-1} determined by Spielhagen et al. (2011) further seaward on Vestnesa Ridge. While the absolute sedimentation rate cannot be constrained more accurately, we note that the sedimentation regime in the study area is characterized by the open slope between two glacial cross-shelf troughs (Vanneste et al., 2007). More than 20 km away from the coast with an uneven shelf that traps terrestrial sediments, the study area is characterized by the absence of turbidites, storm surges, or other processes that would lead to sedimentation pulses as evidenced by the unstratified top of our sediment core. This suggests that the sedimentation rate is variable only on century time scales.

3. Results

3.1. Geophysical Data

Multichannel seismic data from the MASOX site showed high energy scatters within the top 20 ms two-way travel time or about 17 m below the seafloor assuming a seismic velocity for the uppermost glacigenic sediments of 1,700 m s^{-1} (Figure 3). Below ~40 ms two-way travel time, there was a reverse polarity event that stretched ~2,200 m both up and downslope across the margin. The event shoaled about twice as much as the seafloor and was interrupted. Underneath it, the seismic facies were more chaotic than up- and downslope of it.

Because the signal was discontinuous and too shallow, it can be excluded that the reverse polarity event was the seafloor multiple. Reverse polarity, high reflection amplitude, and chaotic seismic facies underneath suggest that the signal was the reflection of a gas-charged horizon at about 20 m depth. This interpretation is consistent with drilling results (Riedel et al., 2018).

The PARASOUND data showed numerous high amplitude reflections within the water column (Figure 4). High amplitude reflections were limited to profile segments of 1–10 m each. They arose from the seafloor reflection, and some reached to depths where they cannot be distinguished from the noise caused by interference of the acoustic signal from the ship. However, most acoustic anomalies were restricted to the lower half of the water column (seafloor to ~200 m) such as the example in Figure 4. The seismic anomalies occurred along a 20-km stretch of the margin and were clustered around the 390-m depth contour, although these anomalies also occurred further landward at shallower water depth where they were less frequent.
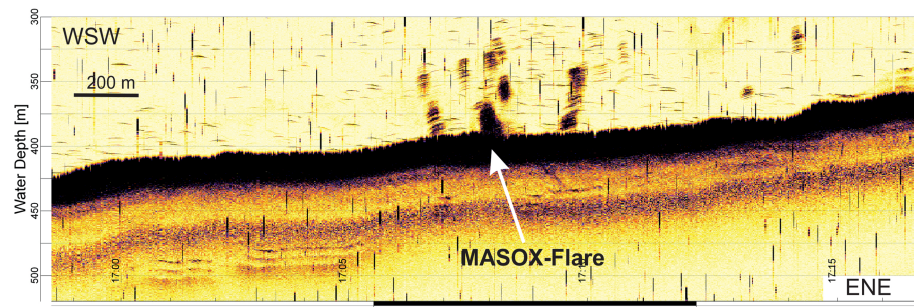
Figure 4. 18 kHz acoustic profile (PARASOUND PHF-signal) crossing the flare at the MASOX site. High amplitude patches in the water column indicate active gas venting.

The acoustic water column anomalies might have been caused by schools of fish or by gas release from the sea floor. Given the direct observation of gas release in this area and the fact that the anomalies can always be traced down to the seabed, we interpret them as the result of acoustic backscatter from gas bubbles. This interpretation is consistent with the interpretations of other studies (Berndt, Feseker, et al., 2014; H. Sahling et al., 2014; Westbrook et al., 2009).

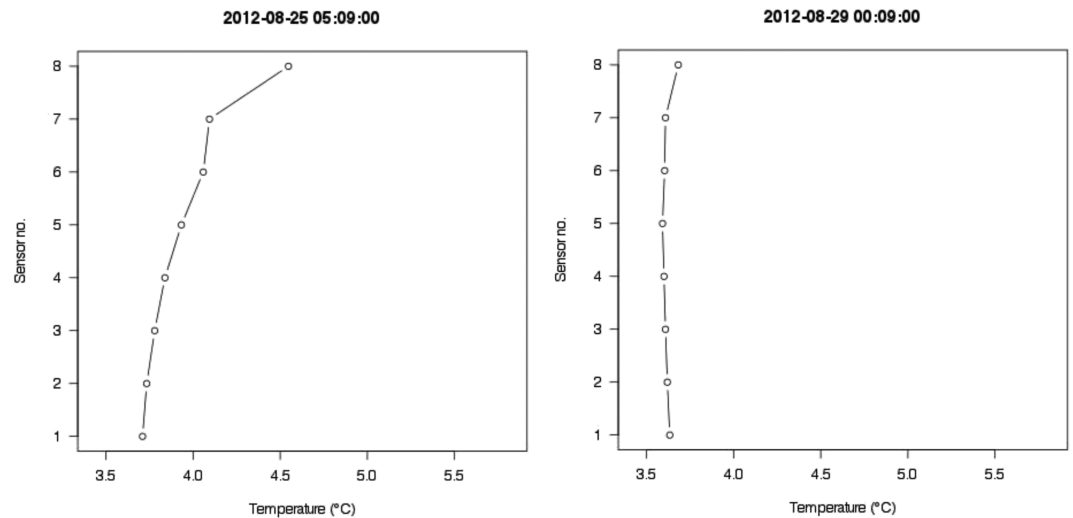### 3.2. Temperature Measurements

Water temperatures during JAGO operations at the peeper site fluctuated around 3.7°C (Table 1). The heat flow probe recorded temperatures between 23 August 2012 9:39 (start of the JAGO dive) and 2 September 2012 14:39 (~2 hr before the probe retrieval). The probe was deployed in the sediment of the peeper site between 23 August 2012 13:24 (deployed) and 2. September 2012 16:50 (retrieved). Hence, the recording started before the probe was deployed in the sediment. During deployment, temperature fluctuated between approximately 3.6°C and 4.6°C at the top sensor (Sensor 8, located close to the sediment-water interface), which we interpreted to be correlated with temperature fluctuations in the water column (Figure 5, Video S1). During deployment time, onshore- and offshore-derived water masses fluctuated in the area leading to small temperature changes at the seafloor (Steinle et al., 2015). Generally, the temperature of the deeper sensors (Sensors 7–2, located between approx. 4.5 and 27 cmbsf) followed changes in the top sensor (Sensor 8), pointing to an equilibration process between fluctuating temperatures in the water column and stable temperatures in the sediment (~3.6°C, Sensor 1, located at ~31.5 cmbsf).

3.3. Peeper Porewater Geochemistry

Sulfate concentrations of most peeper samples were considerably below seawater concentration inside the dialysis bags at the start of the experiment (28.4 mM sulfate) (Figure 6). Further, steep gradients and high concentrations of sulfide (up to ~7,000 μM) and total alkalinity (up to ~18 mEq L^{-1}) were detected. We therefore assume that the deployment time of the peepers (10 days) was sufficient to equilibrate the fluid in the dialysis bag with the pore fluid of the sediment to reflect in situ conditions. Further, based on diffusion coefficients, the diffusion time of most common solutes in seawater is expected to be <3 hr over a distance of 1 cm (as is was the case for the peeper-sediment interface). It should, however, be kept in mind that with a distance of only 1 cm between peeper chambers, some smearing and hence smoothening of concentration profiles is possible.

Sulfate profiles showed a decline from initial seawater concentrations (28.4 mM) at the top to minima of 15–20 mM in deeper layers, indicating that the anion was involved in redox reactions, most likely in sulfate reduction, which was confirmed by simultaneous increase in sulfide and total alkalinity.

Sulfide and total alkalinity showed matching profiles in all peepers, indicating that their production was linked and likely attributed to sulfate reduction. There was a deepening trend of sulfide and total alkalinity peaks laterally from the bacterial mat to the gas vent. Specifically, concentrations reached a maximum at ~12–14 cmbsf at Peepers 1 and 2 (bacterial mat) versus 17–19 cmbsf at Peepers 3 and 4 (tubeworm field) and 34–40 cmbsf at Peepers 5 and 6 (gas vent).

Figure 5. Two selected time points (see time stamp) of vertical temperature measurements during the heat flow probe deployment in the sediment of the peeper site. The distance between the temperature sensors (Sensor 1–8) was 4.5 cm. Sensor 8 was located close to the sediment-water interface. For full temperature recording, see Video S1.

Porewater chloride concentrations in the dialysis bags at the end of the peeper incubation were higher (567–584 mM) than chloride in seawater at the start of the experiment (559 mM) (Figure 6). This reflects a chloride elevation of 1.5–4.3% above initial concentration, which is above the uncertainty of the ion chromatographic measurements (1.2%, determined by IAPSO standard determinations: 557.8 ± 6.6 mM chloride, $n = 11$; IAPSO value provided by manufacturer = 557.9 mM). However, porewater chloride was also elevated (578 mM) in the dialysis bag of the topmost chamber of Peeper 4, which was situated at the sediment-water interface and should therefore represent seawater conditions. Further, sodium (Na^+) concentrations determined by inductively coupled plasma atomic emission spectroscopy in Peepers 2, 4, and 5 did not show a similar elevation above the IAPSO level (439–488 mM in Peeper vs. 474–480 mM in IAPSO, data not shown). We therefore exclude considerable salinity alterations in the porewater that could be related to gas hydrate dissociation or formation.
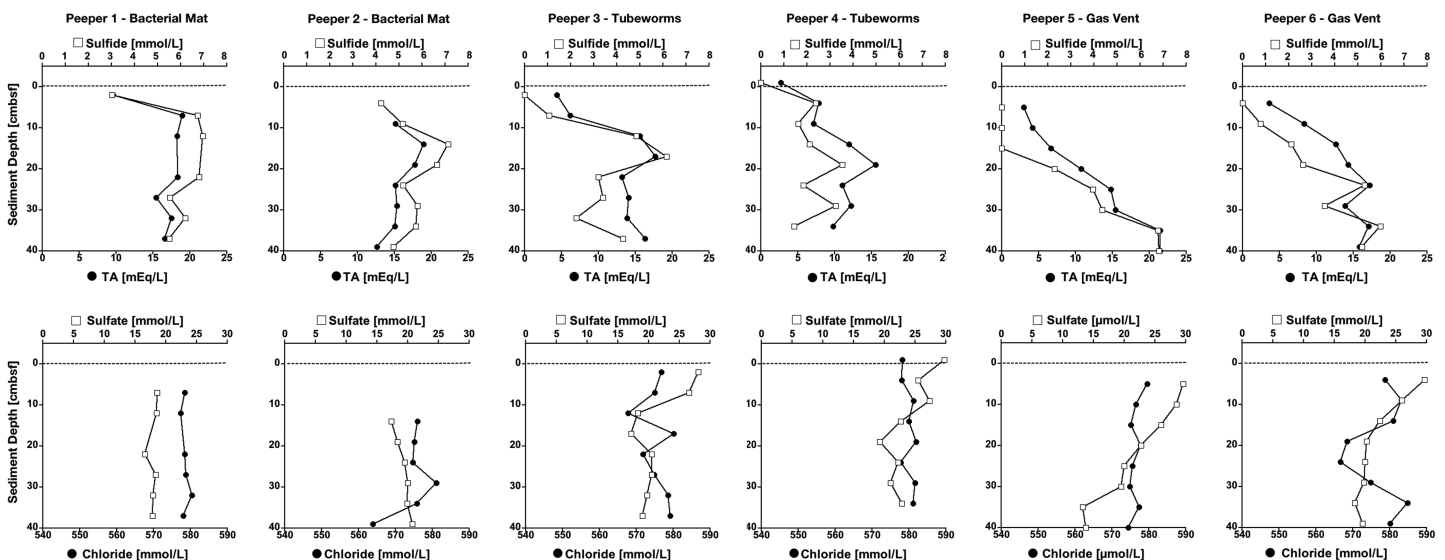
Figure 6. Porewater profiles of sulfide, total alkalinity (TA), sulfate, and chloride of the six peepers deployed at different habitats at the MASOX station: Bacterial mat (Peepers 1 and 2), tubeworms (Peepers 3 and 4), and gas vent (Peepers 5 and 6). The dashed horizontal line marks the sediment-water interface.
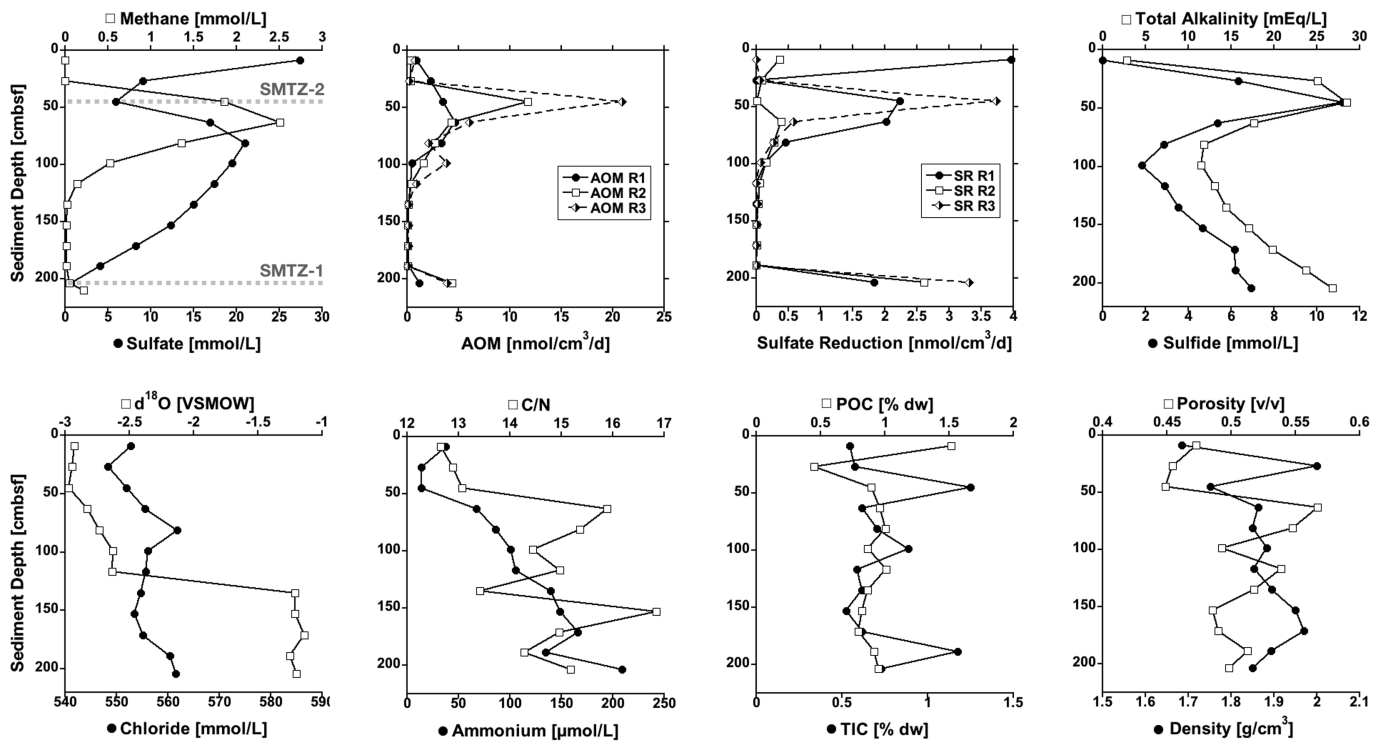
Figure 7. Biogeochemical parameters determined in the gravity corer from the MASOX site. Note that three replicates are shown for anaerobic oxidation of methane (AOM) and sulfate reduction. The dashed horizontal lines in the methane/sulfate graph indicates the approximate depths of the two sulfate-methane transition zones (SMTZ-1 and SMTZ-2).

3.4. Gravity Corer
3.4.1. Biogeochemical Data

Two methane peaks were apparent in the gravity core (Figure 7). The larger peak was located at 63 cmbsf (2.51 mM) with elevated (>0.1 mM) methane concentrations between 45 and 117 cmbsf. We expect that the measured methane concentration represents an underestimation of the true in situ value, because peak concentration reached oversaturation at atmospheric pressure and temperature (saturation ~1 mM at ~4°C, 34 PSU, and 1 atm; Yamamoto et al., 1976) and sediment showed signs of degassing after retrieval (foamy consistency), strongly suggesting gas loss prior to subsampling. The second, smaller methane peak (0.21 mM) was detected at the core catcher depth, i.e., below the deepest core depth (210 cmbsf). Sulfate concentration declined rapidly from the core top (27.4 mM at 9 cmbsf) to 45 cmbsf (5.9 mM) (Figure 7). Below 45 cmbsf, sulfate concentration increased and reached a secondary peak of 21.0 mM at 81 cmbsf. Below this depth, sulfate declined continuously to a minimum of 0.64 mM at 204 cmbsf. Taken together, methane and sulfate profiles revealed two SMTZs: SMTZ-1 at approximately 204 cmbsf and SMTZ-2 at approximately 45 cmbsf. We note that the precise location of the SMTZs might have been missed during selection of sampling intervals.

The AOM rate measurements revealed two peaks of activity, aligned with the SMTZs identified above (Figure 7). AOM at SMTZ-2 ranged from 3.5 to 20.9 nmol cm^{-3} d^{-1} in replicates. AOM rates at SMTZ-1 were lower, ranging between 1.2 and 4.4 nmol cm^{-3} d^{-1}. Sulfate reduction data revealed three peaks of activity in the core (Figure 7). The top peak (0–4.0 nmol cm^{-3} d^{-1}) near the sediment-water interface was likely coupled to organic matter degradation. The second and third peaks were aligned with SMTZ-2 (0.01–3.7 nmol cm^{-3} d^{-1}) and SMTZ-1 (1.8–3.3 nmol cm^{-3} d^{-1}) and thus were likely coupled to AOM. The measured sulfate reduction at SMTZ-2 was one order of magnitude lower compared to AOM. This may be attributable to methodological artifacts created by potential losses of ^{14}C-methane tracer during the incubation due to methane degassing post tracer injection. A diminished ^{14}C-methane pool at the end of the incubation compared to the ^{14}C-methane pool injected would result in overestimation of the methane turnover rate.

Concomitant down core concentration trends for total alkalinity and sulfide were observed (Figure 7), indicating they were produced by the same process. Both parameters peaked at SMTZ-2 (28.5 mEq L^{-1} and 11.2 mM, respectively). A steady increase in concentration below 99 cmbsf toward SMTZ-1 was observed, with a dual secondary maximum at 204 cmbsf (26.8 mEq L^{-1} and 6.9 mM, respectively). These data indicate that total alkalinity and sulfide were byproducts of sulfate-dependent AOM. The ratio of total alkalinity to sulfate was larger than predicted by AOM stoichiometry; however, this may be attributable to sulfide reactivity with iron (precipitation of iron sulfides) in the sediment and a subsequent reduction in porewater values of free sulfide.

Chloride data revealed one minimum concentration depth (548 mM) at 27 cmbsf and two peaks at 81 cmbsf (562 mM) and 204 cmbsf (562 mM) (Figure 7). However, the minimum was only slightly above (1.8%), and the two maxima within (<1%) the uncertainty of the ion chromatographic measurements (1.2%), questioning the relevance of the observations. δ^{18}O of water fluctuated between −2.97 and −2.63 between top and 117 cmbsf. At 135 cmbsf, values sharply increased and fluctuated between −1.14 and −1.21(Figure 7). Causes for this sharp change in in δ^{18}O are currently unknown.

Ammonium showed a small peak (37.8 μM) at the top of the core (9 cmbsf), from where it dropped to values around 13 μM just below (Figure 7). The top peak may be attributable to either tubeworm excretions, since ammonium is the chief nitrogen-containing end product of protein metabolism in aquatic annelids (Quijada-Rodriguez et al., 2017) or to the dissimilatory nitrate reduction to ammonium by filamentous and nitrate-storing sulfur-oxidizing bacteria (Jørgensen & Nelson, 2004; Sommer et al., 2016). Alternatively, or in addition, the ammonium peak could also result from the degradation of labile organic material, which is supported by a peak in POC (1.52% dw) and a relative low C/N ratio (12.7) in this depth. Starting at 63 cmbsf, ammonium values increased almost continuously reaching its maximum (209 μM) at 204 cmbsf likely as a result of organic matter degradation. In accordance, the C/N ratio of dried sediment increases from values around 13 to values mostly >15 below 63 cmbsf (Figure 7).

POC was highest (1.52% dw) at the core top (at 9 cmbsf) and rapidly declined to reach the minimum value of 0.44% dw at 27 cmbsf (Figure 7). Below at 45 cmbsf, POC was relatively uniform, ranging between 0.80 and 1.00% dw. TIC peaked at SMTZ-2 (1.25% dw) with a secondary peak at 189 cmbsf (1.18% dw). At other depths, values ranged between 0.50 and 0.73% dw.

Porosity and density fluctuated throughout the core revealing values between 0.45 and 0.55 and between 1.75 and 2.00 g cm^{-3}, respectively (Figure 7).

3.4.2. Biomarker

Concentrations of archaeol and polar fatty acids 16:1ω5c were low or nondetectable, respectively, in the top sediment layer (9 cmbsf), but increased to maximum values ~0.06 μg g^{-1} wet weight (ww) at 27 cmbsf, which corresponded with the location of SMTZ-2 (Figure 8). Below this depth, both compounds decreased in concentration, but archaeol showed two additional concentration maxima at 117 and 153 cmbsf. The δ^{13}C of archaeol and the polar fatty acids 16:1ω5c were most depleted at the concentration maximum at 27 cmbsf (−110‰ and − 90‰, respectively, Figure 8). The most depleted δ^{13}C value of archaeol, which can be considered as the AOM endmember signal, translates to a $\Delta\delta^{13}$C value of −54‰ when compared to the δ^{13}C value of the dominantly microbial methane source (−56‰; H. Sahling et al., 2014). This magnitude of isotopic depletion of ANME lipids is relatively strong, in particular for ANME-1, when compared to reports from other settings including arctic cold seeps (Lee et al., 2018; Niemann & Elvert, 2008; Niemann et al., 2006; Yao et al., 2019).

Below the depth of maximum δ^{13}C depletion, δ^{13}C of both archaeol and the polar fatty acids 16:1ω5c generally increased and showed irregular negative δ^{13}C excursions trending with concentration at deeper sediment depths. At the SMTZ-1, no notable change was observed in the concentration or δ^{13}C value of archaeol and C16:1ω5 in the SMTZ-1 compared to the overlying layers. It is possible that we missed SMTZ-1 in the biomarker analysis. Sampling intervals were 18 cm thick and were subsampled over their entire depth for different analyses (see Section 2.6).

3.4.3. Molecular Data

On average, 13,420 and 30,577 sequences with median length of 443 base pairs were obtained per sample for bacteria and archaea respectively after quality control (Table S1). Bacterial diversity and OTU richness
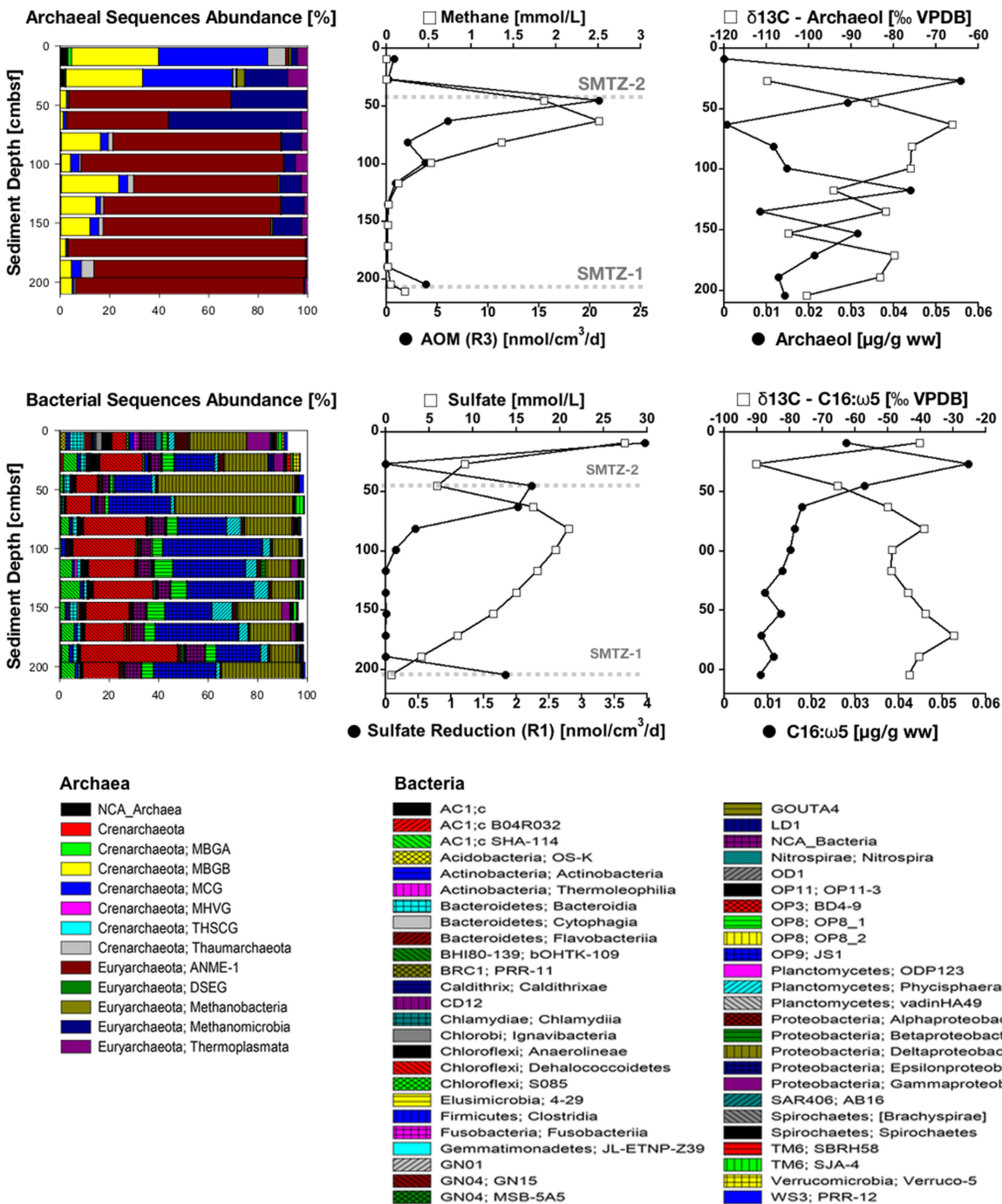
Figure 8. Left: Archaeal (top) and bacterial (bottom) community composition in gravity core samples. Class level relative sequence abundance for all major classes (representing greater than 1% of sample abundance) is displayed. Middle: Depth profiles of methane/AOM (top) and sulfate/sulfate reduction (bottom). Dashed horizontal lines indicate the approximate depths of the sulfate-methane transition zones (SMTZ-1 and SMTZ-2). Only one replicate of AOM and sulfate reduction is displayed (compare with Figure 7). Right: Depth profiles of concentrations and stable carbon isotope ratios (δ^{13}C) of archaeol (top) and C16:1ω5(a) (bottom).

exceed archaea at all depths. Total diversity (bacteria and archaea) was highest at the surface of the core. However, there were secondary peaks in bacterial and archaeal Shannon diversity at 81 cmbsf. Between 144–198 cmbsf and at 117 cmbsf, bacteria and archaea (respectively) had secondary diversity peaks. Bacterial diversity declined through SMTZ-2, and archaeal diversity was lowest at 171 cmbsf.

Bacteria were dominated by *Deltaproteobacteria* in the upper 63 cmbsf (18–48% of sequences) (Figure 8). The highest abundance of *Deltaproteobacteria* sequences (48%) were observed at 45 (SMTZ-2) and secondarily at 63 cmbsf. At both depths, nearly all *Deltaproteobacteria* were affiliated with the *Desulfococcus* genus of strictly anaerobic sulfate-reducing bacteria. *Desulfococcus* abundance dropped precipitously below SMTZ-2, but this group still included 22% of sequences at the bottom of the core (SMTZ-1). Below SMTZ-2, the abundance of OP9-JS1 affiliated sequences ("Atribacteria") rose sharply. This candidate phylum is ubiquitous in anaerobic marine sediment (Nobu et al., 2016). Chloroflexi affiliated with the Dehalococcoidaceae family were uniformly abundant below SMTZ-2 and peaked to 34% of all sequences at 189 cmbsf.

Archaeal abundance through the upper 27 cmbsf was dominated by unidentified *Crenarchaeota* sequences affiliated with the Marine Benthic Group B (30–35%) and the Miscellaneous Crenarchaeota Group (36–44%). Both groups are widespread in marine sedimentary environments, but their biogeochemical role is unknown (Teske & Sørensen, 2008). Through SMTZ-2 (45 and 63 cmbsf), archaeal community structure shifted abruptly toward Euryarchaeota associated with the anaerobic methanotroph ANME-1 candidate clade and the *Methanomicrobia* class (41–65% of sequences). There were 15 *Methanomicrobia*-related OTUs in the data set, but through SMTZ-2, 21–48% were affiliated with an unidentified isolate from the Haakon Mosby Mud Volcano (HMMVBeg-29), which clusters with the ANME-3 (Lösekann et al., 2007). Below SMTZ-2, ANME-1 dominated the core, with peak abundance (96% of sequences) at 171 cmbsf.

3.4.4. Carbonates

Authigenic carbonates were recovered from push cores in shallow sediment (0–10 cmbsf) at the peeper site and pooled (limitation of material) within three different depth sections in the gravity corer (40–50 cmbsf, 60–120 cmbsf, and 120–210 cmbsf). Whereas the surface sampling provided carbonate-dominated concretions, the gravity corer provided chunks of solidified sediment. Relevant data are extracted from Berndt, Feseker, et al. (2014) and presented in Table 2.

The $\delta^{13}C$ of all carbonates ranged between −41.34‰ ± 0.02 (2σ) in solidified sediment and −27.12 ‰ ± 0.02 (2σ) in less to unconsolidated sediment, indicating methane as the dominant carbon source for authigenic carbonate precipitation (Bohrmann et al., 1998; Greinert et al., 2001). The observed variations in $\delta^{13}C$ can be attributed to variable admixtures of methane-derived and sedimentary carbon and different degrees of related consolidation and maturity. The carbonate $\delta^{13}C$ generally fall into the range of porewater $\delta^{13}C$ DIC (−10‰ to −40‰) found in the top 8 meters in this region, accompanied by $\delta^{13}C$ CH_4 values ranging from −50 to −70‰ (VPDB) (Wallmann et al., 2018). Accordingly, carbonate crusts are highly likely a product of AOM coupled to the oxidation of biogenic methane (Greinert et al., 2001). Since the observed $\delta^{18}O$ values of the carbonates were more negative (−3‰ to −1‰ [VSMOW]) than current seawater values in this region (G. A. Schmidt et al., 1999), it is plausible that these carbonates precipitated under the influence of glacial melt water from western Svalbard, which has a mean $\delta^{18}O$ value of −14.7 ‰ (VSMOW) (MacLachlan et al., 2007).

The U–Th ages and estimates presented in Berndt, Feseker, et al. (2014) are generally accompanied by large uncertainties due to low $^{230}Th/^{232}Th$ activity ratios and low carbonate content of the concretions. Additionally, the deduced ages strongly depend on the applied data reduction and correction methods. Nevertheless, based on proposed single-age and isochron results, a general age succession complementary to authigenic precipitation following ongoing low sedimentation implies mean ages of around 17 ka (13.0 ± 5 to 21.7 ± 0.4 ka) for the depth interval 60–120 cmbsf and around 3.4 ka (2.5 ± 0.1 to 5.0 ± 1.1 ka) at today's sediment surface.

The deepest section (120–210 cmbsf) appears to support the age succession with an average age of ~21 ka, but large and strongly overlapping age uncertainties (18.8 ± 13.3 to 22.9 ± 17.2) do not support reliable geochronological interpretation and instead point to potential heterogeneities in the precipitation and consolidation processes. The formation age of the surface concretion indicates an erosive sedimentation regime, and at first sight, the age succession implies no recent or subrecent authigenic carbonate precipitation.

However, a distinct exception in the carbonate chronology is evident in the sediment spanning 40–50 cmbsf. Here, beside a succession matching age of 6.6 ± 0.4 ka for a chunk of highly solidified carbonate-rich sediment, the U–Th analyses indicate an almost recent authigenic precipitation around 0.6 ka (0.55 ± 0.04 to 0.62 ± 0.04 ka), which is in line with the location of SMTZ-2. As methane-derived carbonates above and below this zone are characterized by markedly older ages, a direct vertical advective methane supply
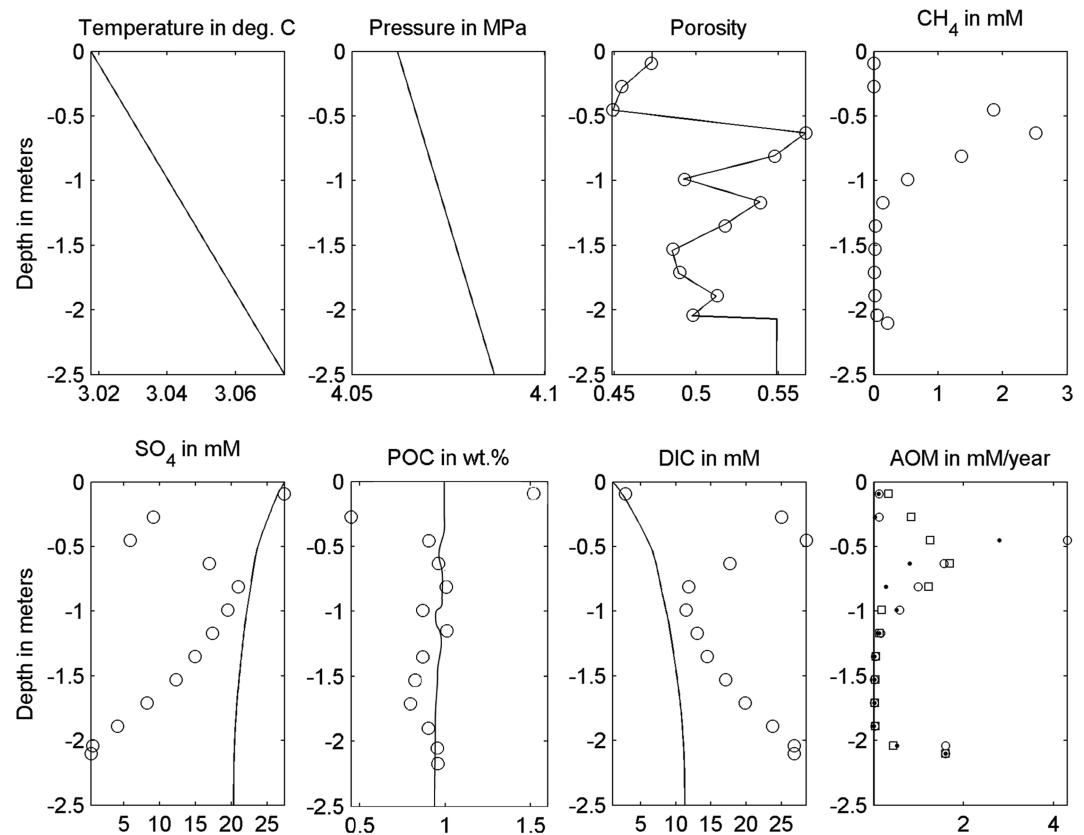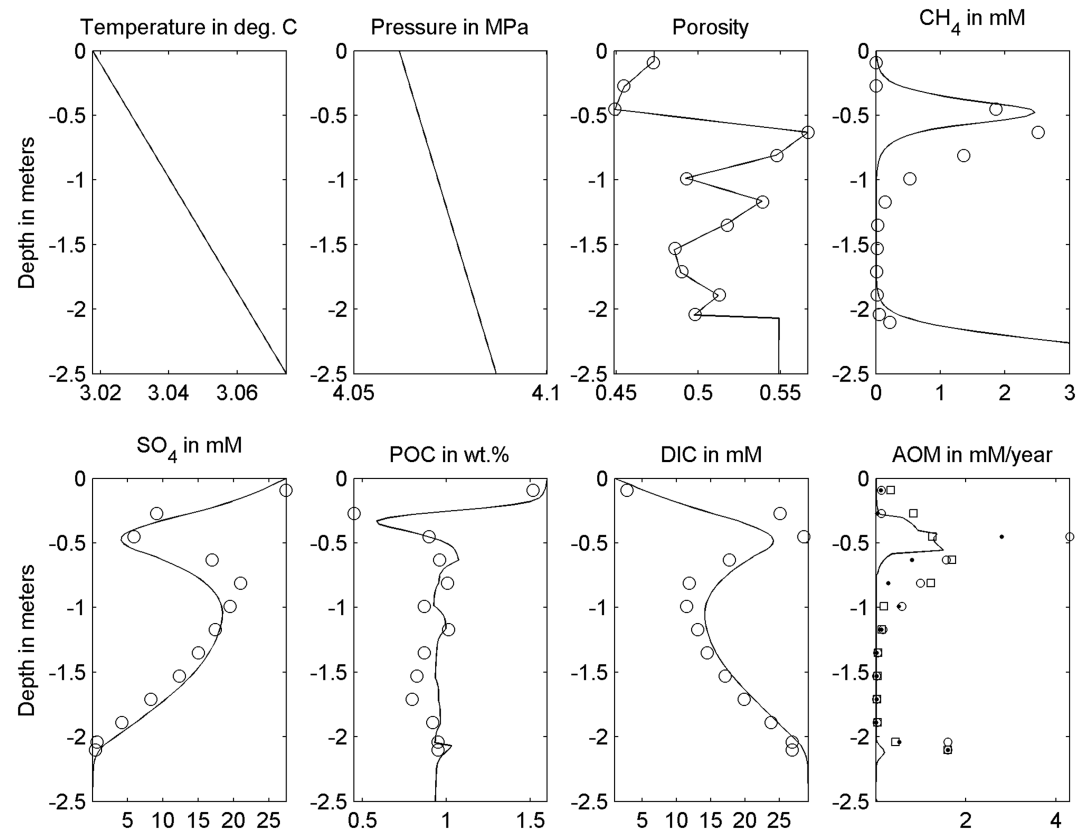
Figure 9. Steady-state scenario obtained after 6,800 years of the simulation time. Dots represent data points (measurements), whereas solid lines depict modeling results. Three replicates are shown for AOM (white dots, black dots, and white squares). In this scenario, no additional in situ POC degradation source of methane was integrated in the model. The amount of biodegraded organic matter is not sufficient to produce the observed methane concentrations; thus, the predicted sulfate profile penetrates deeper into the sediments.

seems an unlikely carbon source. Instead, the record of authigenic carbonate formation indicates a confined nonvertical methane transport within the sediment column.

3.5. Model Results

In a first modeling scenario, we tested if reported methane and sulfate depth profiles were able to be formed exclusively by in situ POC degradation and microbial methanogenesis. This hypothesis could not be confirmed by modeling results (Figure 9), which show that available organic matter is not sufficient to reproduce the measured methane concentrations as the penetration depth of sulfate in this model exceeded the observed values in the sediment core. Figure 9 shows geochemical profiles after the initial 6,800 years of simulation time when the system reached a steady state. This first test supported that the system was not in a steady state at the time of sampling and that an additional methane source is required to explain the measured geochemical observations.

To fit the two SMTZs, additional fluxes of dissolved methane were required. The second scenario (Figure 10) presents modeling that fit the observed methane/sulfate profiles best and includes three steps. Initially, the entire system was simulated for the first 6,158 years without an additional methane source. Next, an additional flux through the lower boundary containing 0.5 mM of dissolved methane per year for the last 145 years was simulated. This methane flux represents vertical advection of dissolved gas entering the system from greater depths as depicted in Figure 10 and is required to develop the deeper SMTZ-1 at ~204 cmbsf. The model was tested with various injection times and rates; however, assuming a constant additional flux no other scenarios could provide a better fit to the data reproducing the measured profiles. In the final step, the development of the upper SMTZ-2 was simulated in parallel with additional

Figure 10. Development of the SMTZs after 6,158 years of the simulation time. Dots represent data points (measurements), whereas solid lines depict modeling results. Three replicates are shown for AOM (white dots, black dots, and white squares). For the last 145 years of simulation, an additional flux of methane (0.5 mM year^{-1}) was prescribed to match methane, sulfate and AOM profiles of the lower SMTZ-1. Additionally, for the last 13 years of simulation, a flux of 1.5 mM year^{-1} and a flux of 4 mM year^{-1} were applied to the upper SMTZ-2 within the uppermost (30.3–40.4 cmbsf) and the deeper (40.4–55.5 cmbsf) intervals, respectively.

dissolved methane flux, which created SMTZ-1. Additional methane supplying the upper part of the system for the next 13 years was required to obtain the measured profiles. To observe good match, this depth section of the profile was divided into two intervals with different nonvertical methane injection rates. This separation was based on trends in the sulfate and methane profiles. The minimum and maximum depths of these two intervals were modified together with the flux volume until the best match was identified. The resulting uppermost interval (30.3–40.4 cmbsf) of SMTZ-2 experienced methane flux with a rate of 1.5 mM year^{-1}, whereas the resulting deeper interval of SMTZ-2 (40.4–55.5 cmbsf) was supplied with an additional 4 mM of methane per year. While these results represent the best match for the two identified intervals, it should be kept in mind that alternative scenarios, including more or less intervals, might be possible.

Since it is rather unlikely that the same rate of methane supply will be maintained in the future, we have further simulated the system behavior after the successful reproduction of the two SMTZs (Figure 10). According to the modeling results, an additional 150 years is required to reestablish the steady-state conditions (data not shown). In this model run, the diffusive supply of sulfate through the water-sediment interface will entirely consume the methane pool and enable sulfate to penetrate into greater depths.

4. Discussion

4.1. Biogeochemical Zonation of the Peeper Site

Geochemical profiles of sulfide and total alkalinity (Figure 6), specifically, the depth where both parameters peaked, indicate a shoaling of the AOM activity maximum from the gas vent toward the bacterial mat. Free

gas escape observed only at the periphery of the peeper site further suggests that gas discharge was largely prevented below the central bacterial mat and the surrounding tubeworm field. Prevention of gas discharge could be created by different structures in the sediments that are impermeable for free gas, including gas hydrates and cemented mixtures of carbonates and cobbles. Strong sediment heterogeneity was indicated in the area by ultrahigh-resolution seismic data (Ker et al., 2014) and controlled-source electromagnetic data (Goswami et al., 2016). Further, large outcropping carbonate platforms were discovered in the study area (Berndt, Feseker, et al., 2014), and sediment subsampling at the peeper site was prevented by solid structures in the surface sediment. Sediment heterogeneity caused by hydrates and carbonates has been noted to cause strong small-scale variability of AOM activity and chemosynthetic communities in surface sediments (Sahling et al., 2002; Treude et al., 2003).

Different observations could entertain the idea of gas hydrate occurrence in the sediment. The presence of free gas within the GHSZ, as confirmed by gas bubble releases (visual observation at Peepers 5 and 6 [Figure S1] and PARASOUND reflections [Figure 4]) and the presence of a gas-charged horizon at about 20 mbsf (geophysical reverse polarity [Figure 3]) provide evidence that sufficient free gas was present to form gas hydrate. Water temperature recording over a 2-year period at the seafloor close to the peeper site directly prior to sampling (MASOX observatory; Berndt, Feseker, et al., 2014) showed that the site provided conditions for gas hydrate formation in the surface sediments from roughly April to mid-June 2012, when temperatures below the gas hydrate stability limit were reached (+3.0°C at 400 m; Berndt, Feseker, et al., 2014; Riedel et al., 2018). After mid-June, water temperatures increased above +3.0°C at the seafloor, which likely lead to a gradual reduction of the GHSZ within the top ~5 m of the surface sediment (Berndt, Feseker, et al., 2014). However, in situ water (~3.8°C, Table 1) and sediment temperature (3.6°C, Figure 5, Video S1) at the peeper site revealed that conditions were not favorable for gas hydrate formation in the surface sediment at the time of sampling, and porewater chloride profiles provided no indication for hydrate dissociation. We therefore conclude that no hydrates were present in depths sampled at the peeper site. It is, however, possible that residual hydrates persisted in the top 5–10 m, beneath the penetration depth of our instruments, and supplied methane to the overlying chemosynthetic communities. Recent studies revealed new evidences for seasonal gas hydrate formation and dissociation in the study area, which causes temperature-driven fluctuations of gas release along the upper continental slope depending on the location of the GHSZ (Ferré et al., 2020; Veloso-Alarcón et al., 2019).

Irrespective of the methane sources, we noticed strong lateral heterogeneity and restricted gas discharge at the peeper site. This observation will be combined with the discussion of the gravity core and model results (Section 4.2) toward a unifying hypothesis (Section 4.3).

4.2. Reconstruction of Processes in the Gravity Core Sediment

The 1D model run, which reproduced the observed geochemical profiles, predicts that SMTZ-1 was formed by vertical methane flux from a deeper source ~145 years before sampling, while SMTZ-2 was induced by nonvertical methane transport introduced ~13 years before sampling. In this section, model results are compared to observational data (microbial taxonomy, biomarkers, and carbonates) from the gravity core.

Observational data from this study support a recent formation of the shallow SMTZ-2. The abundance of diagnostic biomarkers derived from both, archaea and SRB peaked in close proximity to SMTZ-2. Furthermore, both classes of compounds were isotopically depleted ($\delta^{13}C$ values below −80‰), indicative of methane-derived carbon assimilation into microbial biomass (Figure 8) (Hinrichs et al., 1999). Further, OTUs are related to *Desulfococcus*, ANME-1, methanomicrobiota, and ANME-3 peak in abundance at SMTZ-2. Authigenic carbonates show their youngest age (~600 years before sampling) within SMTZ-2, which can be best explained by nonvertical methane transport since carbonates above and below SMTZ-2 are much older. However, an estimated age of 600 years for carbonates at SMTZ-2 is not commensurate with the modeled age of the zone (13 years). It is likely that younger carbonates precipitated around older ones, thereby masking their actual age.

Below SMTZ-2, the interpretation of methane-related parameters is not as straightforward. If both SMTZs were the only SMTZs ever present in the sediment, a discontinuity of methane-related parameters between the two zones is expected. However, the presence of microbial biomarkers and sequences indicative of anaerobic methanotrophs and methane-derived authigenic carbonates continue below SMTZ-2, although in

lower abundance and with a higher age, respectively. Possible explanations are that nonvertical methane injections occurred at several depths below SMTZ-2 in the past or that the methane flux at SMTZ-1 fluctuated over time, periodically moving SMTZ-1 closer to the sediment surface when methane flux was higher. Regardless of past flux regimes, biogeochemical data (methane, sulfate, AOM, and sulfate reduction) show that the second older point of methane consumption in the gravity core is currently located at what we define as SMTZ-1.

4.3. Possible Causes for Nonvertical Methane Injection at SMTZ-2

Accepting some positioning uncertainty, we are confident that the gravity core was taken proximate to the peeper site. A comparison of sulfide profiles between the peeper and the gravity corer site excludes the possibility that the core was taken in the center of the peeper site at locations with relatively shallow AOM activity (bacterial mat and tubeworm field). Here, sulfide concentrations ranged between 2 and 6 mM in the top 10 cmbsf, while no sulfide was detected at 9 cmbsf in the gravity core. It is more likely that the gravity core was taken at the periphery of the peeper site, because sulfide concentration at 26 cmbsf (~6 mM) agreed with sulfide concentrations found between 20 and 30 cmbsf at the gas vent peepers. If the gravity corer was deployed at the periphery of the peeper site, and if gas discharge was largely prevented in the center and released at the periphery, the gravity core could have been impacted by methane transport detoured laterally underneath the peeper site, which resulted in the formation of SMTZ-2.

An alternative explanation for the formation of SMTZ-2 could be injection of methane through recently formed nonvertical sediment fractures (Impey et al., 1997). It is notable that sediment fractures leading to nonvertical methane influx and buildup of AOM communities were found at three seep sites, two of which are at nearby artic locations, Gas Hydrate Pingo and Vestnesa Ridge (Briggs et al., 2011; Gründger et al., 2019; Yao et al., 2019). The observation that methane supply was much shallower at the peeper site compared to SMTZ-1 in the gravity core further indicates a complex fluid advection system at the MASOX site.

4.4. Response Time of the Benthic Methane Filter

This study provides insight into the response time of the methanotrophic microbial community to nonvertical methane injections caused by either blockages of vertical gas flow or transport trough newly formed sediment fractures. The injected methane propagated sideways into methane-pristine sediments creating a nonsteady state SMTZ, which takes 100 years or more to reestablish steady-state conditions. The 1D model suggests the injection started ~13 years before sampling. Despite this relatively short time frame, the AOM community responded to the methane injection as demonstrated by different molecular biological, biomarker, and biogeochemical data. Specifically, although concentrations of the ANME biomarker archaeol and AOM rates were 1–2 orders of magnitude lower compared to methane seeps like Hydrate Ridge (Elvert et al., 2005), the response intensity was consistent with suggested nonvertical methane flux (1.5 mM year^{-1}), which was also 1–2 orders of magnitude lower than Hydrate Ridge (Torres et al., 2002; Treude et al., 2003). Hence, the microbial response appears commensurate with methane supply. A similar response time was reported from a man-made methane blowout in the North Sea (Wilfert et al., 2015). However, given the presence of ANME OTUs and biomarkers between SMTZ-2 and SMTZ-1, as well as methane-derived carbonates predating the nonvertical methane injection, it is possible that the sediment was already primed with a methanotrophic community poised to respond to new methane delivery. ANMEs have very slow growth rates (doubling times of 4–7 months under laboratory conditions; Nauhaus et al., 2007) and are relatively tolerant to methane shortage even after years of storage in the laboratory without methane supply (T. Treude, pers. observ.). This resilient capability could be advantageous to control methane emissions in areas with fluctuating methane fluxes, in particular seasonal fluctuations driven by up and down movements of the GHSZ as observed in the study area (Berndt, Feseker, et al., 2014; Ferré et al., 2020; Veloso-Alarcón et al., 2019].

References

Archer, D. (2007). Methane hydrate stability and anthropogenic climate change. *Biogeosciences Discussions*, *4*(2), 993–1057. https://doi.org/10.5194/bgd-4-993-2007

Baumberger, T., Embley, R. W., Merle, S. G., Lilley, M. D., Raineault, N. A., & Lupton, J. E. (2018). Mantle-derived helium and multiple methane sources in gas bubbles of cold seeps along the Cascadia Continental Margin. *Geochemistry, Geophysics, Geosystems*, *19*(11), 4476–4486.

Berndt, C., Feseker, T., Treude, T., Krastel, S., Liebetrau, V., Niemann, H., et al. (2014). Temporal constraints on hydrate-controlled methane seepage off Svalbard. *Science*, *343*(6168), 284–287. https://doi.org/10.1126/science.1246298

Berndt C., Dumke, I., Feseker, T., Graves, C., Franek, P., Hissmann, K., et al. (2014). Fluid dynamics and slope stability offshore W-Spitsbergen: Effect of bottom water warming on gas hydrates and slope stability - Cruise No. MSM21/4 - August 12 - September 11, 2012 - Reykjavik (Iceland) - Emden (Germany) in MARIA S. MERIAN-Berichte, edited, p. 96, DFG-Senatskommission für Ozeanographie, Bremen. https://doi.org/10.2312/cr_msm21_4

Biastoch, A., Treude, T., Rüpke, L. H., Riebesell, U., Roth, C., Burwicz, E. B., et al. (2011). Rising Arctic Ocean temperatures cause gas hydrate destabilization and ocean acidification. *Geophys. Res. Let.*, *38*, L08602. https://doi.org/10.1029/02011GL047222

Boetius, A., & Wenzhöfer, F. (2013). Seafloor oxygen consumption fuelled by methane from cold seeps. *Nature Geoscience*, *6*(9), 725.

Bohrmann, G., Greinert, J., Suess, E., & Torres, M. (1998). Authigenic carbonates from the Cascadia subduction zone and their relation to gas hydrate stability. *Geology*, *26*(7), 647–650.

Boswell, R., & Collett, T. S. (2011). Current perspectives on gas hydrate resources. *Energy Environ. Sci.*, *4*(4), 1206–1215.

Briggs, B. R., Pohlman, J. W., Torres, M., Riedel, M., Brodie, E. L., & Colwell, F. S. (2011). Macroscopic biofilms in fracture-dominated sediment that anaerobically oxidize methane. *Applied and Environmental Microbiology*, *77*(19), 6780–6787. https://doi.org/10.1128/AEM.00288-11

Bruevich, S. V. (1944). Determination of alkalinity in small volumes of seawater using direct filtration. *Manual on Chemical Studies of Seawater*.

Buffett, B., & Archer, D. (2004). Global inventory of methane clathrate: Sensitivity to changes in the deep ocean. *Earth and Planetary Science Letters*, *227*, 185–199.

Burwicz, E., & Rüpke, L. (2019). Thermal state of the Blake ridge gas hydrate stability zone (GHSZ)—Insights on gas hydrate dynamics from a new multi-phase numerical model. *Energies*, *12*(17), 3403.

Burwicz, E. B., Rüpke, L. H., & Wallmann, K. (2011). Estimation of the global amount of submarine gas hydrates formed via microbial methane formation based on numerical reaction-transport modeling and a novel parameterization of Holocene sedimentation. *Geochim. Cosmochim. Acta*, *75*, 4562–4576.

Caporaso, J. G., Kuczynski, J., Stombaugh, J., Bittinger, K., Bushman, F. D., Costello, E. K., et al. (2010). QIIME allows analysis of high-throughput community sequencing data. *Nature Methods*, *7*(5), 335–336. https://doi.org/10.1038/nmeth.f.303

Cheng, H., Edwards, R. L., Hoff, J., Gallup, C. D., Richards, D. A., & Asmerom, Y. (2000). The half-lives of uranium-234 and thorium-230. *Chemical Geology*, *169*(1–2), 17–33.

Cline, J. D. (1969). Spectrophometric determination of hydrogen sulfide in natural waters. *Limnology and Oceanography*, *14*, 454–458.

Comeau, A. M., Li, W. K., Tremblay, J. E., Carmack, E. C., & Lovejoy, C. (2011). Arctic Ocean microbial community structure before and after the 2007 record sea ice minimum. *PLoS ONE*, *6*, e27492.

Cordes, E. E., Arthur, M. A., Shea, K., Arvidson, R. S., & Fisher, C. R. (2005). Modeling the mutualistic interactions between tubeworms and microbial consortia. *PLoS Biology*, *3*(3), 1–10.

Crémière, A., Lepland, A., Chand, S., Sahy, D., Condon, D. J., Noble, S. R., et al. (2016). Timescales of methane seepage on the Norwegian margin following collapse of the Scandinavian Ice Sheet. *Nature communications*, *7*. https://doi.org/10.1038/ncomms11509

Dattagupta, S., Telesnicki, G., Luley, K., Predmore, B., McGinley, M., & Fisher, C. R. (2007). Submersible operated peepers for collecting porewater from deep-sea sediments. *Limnology and Oceanography: Methods*, *5*, 263–268.

Edgar, R. C. (2013). UPARSE: Highly accurate OTU sequences from microbial amplicon reads. *Nature Methods*, *10*(10), 996–998. https://doi.org/10.1038/nmeth.2604

Elvert, M., Boetius, A., Knittel, K., & Jørgensen, B. B. (2003). Characterization of specific membrane fatty acids as chemotaxonomic markers for sulfate-reducing bacteria involved in anaerobic oxidation of methane. *Geomicrobiology Journal*, *20*(4), 403–419. https://doi.org/10.1080/01490450303894

Elvert, M., Hopmans, E. C., Treude, T., Boetius, A., & Suess, E. (2005). Spatial variations of methanotrophic consortia at cold methane seeps: Implications from a high-resolution molecular and isotopic approach. *Geobiology*, *3*(195–209).

Ferré, B., Jansson, P. G., Moser, M., Serov, P., Portnov, A., Graves, C. A., et al. (2020). Reduced methane seepage from Arctic sediments during cold bottom water conditions. *Nature Geoscience*, 1-5.

Feseker, T., Wetzel, G., & Heesemann, B. (2012). Introducing the T-Stick: A new device for high precision in situ sediment temperature profile measurements. *Limnology and Oceanography: Methods*, *10*(1), 31–40.

Fietzke, J., Liebetrau, V., Eisenhauer, A., & Dullo, C. (2005). Determination of uranium isotope ratios by multi-static MIC-ICP-MS: Method and implementation for precise U- and Th-series isotope measurements. *Journal of Analytical Atomic Spectrometry*, *20*(5), 395–401.

Goswami, B. K., Weitemeyer, K. A., Minshull, T. A., Sinha, M. C., Westbrook, G. K., & Marín-Moreno, H. (2016). Resistivity image beneath an area of active methane seeps in the west Svalbard continental slope. *Geophysical Supplements to the Monthly Notices of the Royal Astronomical Society*, *207*(2), 1286–1302.

Grasshoff, K., Ehrhardt, M., & Kremling, K. (1999). *Methods of seawater analysis*. Wiley-VCH Verlag GmbH: Weinheim.

Graves, C. A., James, R. H., Sapart, C. J., Stott, A. W., Wright, I. C., Berndt, C., et al. (2017). Methane in shallow subsurface sediments at the landward limit of the gas hydrate stability zone offshore western Svalbard. *Geochimica et Cosmochimica Acta*, *198*, 419–438.

Graves, C. A., Steinle, L., Rehder, G., Niemann, H., Connelly, D. P., Lowry, D., et al. (2015). Fluxes and fate of dissolved methane released at the seafloor at the landward limit of the gas hydrate stability zone offshore western Svalbard. *J. Geophys. Res.:Oceans*, *120*(9), 6185–6201.

Greinert, J., Bohrmann, G., & Suess, E. (2001). *Gas hydrate-associated carbonates and methane-venting at Hydrate Ridge: Classification, distribution, and origin of authigenic lithologies*. Union, Washington, D.C.: Am. Geophys.

Gründger, F., Carrier, V., Svenning, M. M., Panieri, G., Vonnahme, T. R., Klasek, S., & Niemann, H. (2019). Methane-fuelled biofilms predominantly composed of methanotrophic ANME-1 in Arctic gas hydrate-related sediments. *Scientific Reports*, *9*(1), 1–10.

Hamdan, L. J., Coffin, R. B., Sikaroodi, M., Greinert, J., Treude, T., & Gillevet, P. M. (2013). Ocean currents shape the microbiome of Arctic marine sediments. *ISME Journal*, *7*(4), 685–696. https://doi.org/10.1038/ismej.2012.143

Hamdan, L. J., Salerno, J. L., Reed, A., Joye, S. B., & Damour, M. (2018). The impact of the Deepwater Horizon blowout on historic shipwreck-associated sediment microbiomes in the northern Gulf of Mexico. *Scientific Reports*, *8*(1), 9057. https://doi.org/10.1038/s41598-018-27350-z

Hantschel, T., & Kauerauf, A. I. (2009). Fundamentals of basin and petroleum systems modeling. Springer Science & Business Media.

Hester, K. C., & Brewer, P. G. (2009). Clathrate hydrates in nature. *Ann. Rev. Marine Sci.*, *1*, 303–327.

Hinrichs, K.-U., Hayes, J. M., Sylva, S. P., Brewer, P. G., & De Long, E. F. (1999). Methane-consuming archaebacteria in marine sediments. *nature*, *398*, 802–805.

Impey, M. D., Grindrod, P., Takase, H., & Worgan, K. J. (1997). A capillary network model for gas migration in low-permeability media. *SIAM Journal on Applied Mathematics*, 597-608.

Stocker, T. F., Qin, D., Plattner, G.-K., Tignor, M. M. B., Allen, S. K., Boschung, J., Nauels, A., Xia, Y., Bex, V., & Midgley, P. M. (2013).. Climate change 2013: The physical science basis. Contribution of working group I to the fifth assessment report of the intergovernmental panel on climate change, 1535. *Cambridge University Press*.

Iversen, N., & Jørgensen, B. B. (1985). Anaerobic methane oxidation rates at the sulphate-methane transition in marine sediments from Kattegat and Skagerrak (Denmark). *Limnology and Oceanography*, *30*(5), 944–955.

James, R. H., Bousquet, P., Bussmann, I., Haeckel, M., Kipfer, R., Leifer, I., et al. (2016). Effects of climate change on methane emissions from seafloor sediments in the Arctic Ocean: A review. *Limnology and Oceanography*, *61*(S1), S283–S299. https://doi.org/10.1002/lno.10307

Jørgensen, B. B., & Nelson, D. C. (2004). Sulfide oxidation in marine sediments: Geochemistry meets microbiology. *Geological Society of America, Special Paper*, *379*, 63–81.

Jørgensen, B. B., Weber, A., & Zopfi, J. (2001). Sulphate reduction and anaerobic methane oxidation in Black Sea sediments. *Deep-Sea Res. I*, *48*, 2097–2120.

Joye, S. B., Boetius, A., Orcutt, B. N., Montoya, J. P., Schulz, H. N., Erickson, M. J., & Logo, S. K. (2004). The anaerobic oxidation of methane and sulfate reduction in sediments from Gulf of Mexico cold seeps. *Chemical Geology*, *205*(3-4), 219–238. https://doi.org/10.1016/j.chemgeo.2003.12.019

Kallmeyer, J., Ferdelman, T. G., Weber, A., Fossing, H., & Jørgensen, B. B. (2004). A cold chromium distillation procedure for radiolabeled sulfide applied to sulfate reduction measurements. *Limnology and Oceanography: Methods*, *2*, 171–180.

Ker, S., Le Gonidec, Y., Marsset, B., Westbrook, G. K., Gibert, D., & Minshull, T. A. (2014). Fine-scale gas distribution in marine sediments assessed from deep-towed seismic data. *Geophysical Journal International*, *196*(3), 1466–1470.

Kirschke, S., Bousquet, P., Ciais, P., Saunois, M., Canadell, J. G., Dlugokencky, E. J., et al. (2013). Three decades of global methane sources and sinks. *Nature Geosci.*, *6*(10), 813.

Knittel, K., & Boetius, A. (2009). Anaerobic oxidation of methane: Progress with an unknown process. *Annual Review of Microbiology*, *63*, 311–334. https://doi.org/10.1146/annurev.micro.61.080706.093130

Kretschmer, K., Biastoch, A., Rüpke, L., & Burwicz, E. (2015). Modeling the fate of methane hydrates under global warming. *Global Biogeochemical Cycles*, *29*(5), 610–625.

Krey, V., Canadell, J. G., Nakicenovic, N., Abe, Y., Andruleit, H., Archer, D., et al. (2009). Gas hydrates: Entrance to a methane age or climate threat? *Environmental Research Letters*, *4*(3), 034007. https://doi.org/10.1088/1748-9326/1084/1083/034007

Kvenvolden, K. (1993). A primer on gas hydrates. *US Geological Survey*, *1570*, 279–291.

Kvenvolden, K. A. (1988). Methane hydrate—A major reservoir of carbon in the shallow geosphere? *Chemical Geology*, *71*(1-3), 41–51. https://doi.org/10.1016/0009-2541(88)90104-0

Lee, D.-H., Kim, J. H., Lee, Y. M., Stadnitskaia, A., Jin, Y. K., Niemann, H., et al. (2018). Biogeochemical evidence of anaerobic methane oxidation on active submarine mud volcanoes on the continental slope of the Canadian Beaufort Sea.

Liebetrau, V., Eisenhauer, A., & Linke, P. (2010). Cold seep carbonates and associated cold-water corals at the Hikurangi Margin, New Zealand: New insights into fluid pathways, growth structures and geochronology. *Marine Geology*, *272*(1–4), 307–318.

Ludwig, K. R. (2008). Isoplot 3.7: A Geochronological Toolkit for Microsoft Excel. Berkeley Geochronology Center Spec. Publ., 4.

Lösekann, T., Knittel, K., Nadalig, T., Fuchs, B., Niemann, H., Boetius, A., & Amann, R. (2007). Diversity and abundance of aerobic and anaerobic methane oxidizers at the Haakon Mosby mud volcano, Barents Sea. *Applied and Environmental Microbiology*, *73*(10), 3348–3362.

MacLachlan, S. E., Cottier, F. R., Austin, W. E. N., & Howe, J. A. (2007). The salinity: Delta O-18 water relationship in Kongsfjorden, western Spitsbergen. *Polar Research*, *26*, 160–167.

Marín-Moreno, H., Minshull, T. A., Westbrook, G. K., & Sinha, B. (2015). Estimates of future warming-induced methane emissions from hydrate offshore west Svalbard for a range of climate models. *Geochem., Geophys., Geosys.*, *16*(5), 1307–1323.

Marín-Moreno, H., Minshull, T. A., Westbrook, G. K., Sinha, B., & Sarkar, S. (2013). The response of methane hydrate beneath the seabed offshore Svalbard to ocean warming during the next three centuries. *Geophysical Research Letters*, *40*(19), 5159–5163.

Mau, S., Römer, M., Torres, M. E., Bussmann, I., Pape, T., Damm, E., et al. (2017). Widespread methane seepage along the continental margin off Svalbard-from Bjørnøya to Kongsfjorden. *Scientific Reports*, *7*, 42,997.

Moss, C. W., & Lambert-Fair, M. A. (1989). Location of double bonds in monounsaturated fatty acids of campylobacter cryaerophila with dimethyl disulfide derivatives and combined gas chromatography-mass spectrometry. *J. Clinic. Microbiol.*, *27*(7), 1467–1470.

Myhre, C. L., Ferré, B., Platt, S. M., Silyakova, A., Hermansen, O., Allen, G., et al. (2016). Extensive release of methane from Arctic seabed west of Svalbard during summer 2014 does not influence the atmosphere. *Geophysical Research Letters*, *43*(9), 4624–4631.

Nauhaus, K., Albrecht, M., Elvert, M., Boetius, A., & Widdel, F. (2007). In vitro cell growth of marine archaeal-bacterial consortia during anaerobic oxidation of methane with sulfate. *Environmental Microbiology*, *9*(1), 187–196. https://doi.org/10.1111/j.1462-2920.2006.01127.x

Nichols, P. D., Guckert, J. B., & White, D. C. (1986). Determination of monounsaturated fatty acid double-bond position and geometry for microbial monocultures and complex consortia by capillary GC-MS of their dimethyl disulphide adducts. *Journal of Microbiological Methods*, *5*(1), 49–55.

Niemann, H., & Elvert, M. (2008). Diagnostic lipid biomarker and stable carbon isotope signatures of microbial communities mediating the anaerobic oxidation of methane with sulphate. *Organic Geochemistry*, *39*(12), 1668–1677.

Niemann, H., Elvert, M., Hovland, M., Orcutt, B., Judd, A., Suck, I., et al. (2005). Methane emission and consumption at a North Sea gas seep (Tommeliten area). *Biogeosciences*, *2*, 334–351.

Niemann, H., Lösekann, T., de Beer, D., Elvert, M., Nadalig, T., Knittel, K., et al. (2006). Novel microbial communities of the Haakon Mosby mud volcano and their role as a methane sink. *Nature*, *443*(7113), 854–858. https://doi.org/10.1038/nature05227

Nisbet, E. G. (1989). Some northern sources of atmospheric methane: Production, history, and future implications. *Canadian Journal of Earth Sciences*, *26*(8), 1603–1611.

Nobu, M. K., Dodsworth, J. A., Murugapiran, S. K., Rinke, C., Gies, E. A., Webster, G., et al. (2016). Phylogeny and physiology of candidate phylum 'Atribacteria' (OP9/JS1) inferred from cultivation-independent genomics. *The ISME Journal*, *10*(2), 273–286. https://doi.org/10.1038/ismej.2015.97

Pavlova, G. Y., Tishchenko, P. Y., Volkova, T. I., Dickson, A., & Wallmann, K. (2008). Intercalibration of Bruevich's method to determine the total alkalinity in seawater. *Oceanology*, *48*(3), 438–443.

Platt, S. M., Eckhardt, S., Ferré, B., Fisher, R. E., Hermansen, O., Jansson, P., et al. (2018). Methane at Svalbard and over the European Arctic Ocean. *Atmospheric Chemistry and Physics*, *18*(23), 17,207–17,224.

Quijada-Rodriguez, A. R., Adlimoghaddam, A., & Weihrauch, D. (2017). Nitrogen excretion in nematodes, platyhelminthes, and annelids. In *Acid-base balance and nitrogen excretion in invertebrates* (pp. 127–150). Cham: Springer.

Reagan, M. T., & Moridis, G. J. (2009). Large-scale simulation of methane hydrate dissociation along the West Spitsbergen margin. *Geophysical Research Letters*, *36*(23).

Riedel, M., Wallmann, K., Berndt, C., Pape, T., Freudenthal, T., Bergenthal, M., et al. (2018). In situ temperature measurements at the Svalbard continental margin: Implications for gas hydrate dynamics. *Geochem., Geophys., Geosys.*, *19*(4), 1165–1177.

Ruppel, C. D. (2011). Methane hydrates and contemporary climate change. *Nature Eduction Knowledge*, *2*(12), 12.

Ruppel, C. D., & Kessler, J. D. (2017). The interaction of climate change and methane hydrates. *Reviews of Geophysics*, *55*(1), 126–168.

Sahling, H., Masson, D. G., Ranero, C. R., Hühnerbach, V., Weinrebe, W., Klaucke, I., et al. (2008). Fluid seepage at the continental margin offshore Costa Rica and southern Nicaragua. *Geochem. Geophys. Geosyst.*, *9*(Q05S05). https://doi.org/10.1029/2008GC001978

Sahling, H., Rickert, D., Raymond, W. L., Linke, P., & Suess, E. (2002). Macrofaunal community structure and sulfide flux at gas hydrate deposits from the Cascadia convergent margin, NE Pacific. *Marine Ecology Progress Series*, *231*, 121–138.

Sahling, H., Römer, M., Pape, T., Bergès, B., dos Santos Fereirra, C., Boelmann, J., et al. (2014). Gas emissions at the continental margin west of Svalbard: Mapping, sampling, and quantification. *Biogeosciences*, *11*(21).

Salerno, J., Little, B., Lee, J., & Hamdan, L. J. (2018). Exposure to crude oil and chemical dispersant may impact marine microbial biofilm composition and steel corrosion. *Frontiers in Marine Science*, *5*(196).

Sarkar, S., Berndt, C., Minshull, T. A., Westbrook, G. K., Klaeschen, D., Masson, D. G., et al. (2012). Seismic evidence for shallow gas-escape features associated with a retreating gas hydrate zone offshore West Svalbard. *Journal of Geophysical Research: Solid Earth*, *117*(B9).

Schmidt, C., Burwicz, E., Hensen, C., Wallmann, K., Martinez-Loriente, S., & Gracia, E. (2018). Genesis of mud volcano fluids in the Gulf of Cadiz using a novel basin-scale model approach. *Geochimica et Cosmochimica Acta*, *243*, 186–204.

Schmidt, G. A., Bigg, G. R., & Rohling, E. J. (1999). Global seawater oxygen-18 Database—v1.22, edited. https://data.giss.nasa.gov/o18data/

Shakhova, N., Semiletov, I., Leifer, I., Sergienko, V., Salyuk, A., Kosmach, D., et al. (2014). Ebullition and storm-induced methane release from the east Siberian Arctic shelf. *Nature Geoscience*, *7*(1), 64.

Shakhova, N., Semiletov, I., Salyuk, A. N., Yusupov, V., Kosmach, D. A., & Gustafsson, Ö. (2010). Extensive methane venting to the atmosphere from sediments of the east Siberian Arctic shelf. *Science*, *327*(5970), 1246–1250. https://doi.org/10.1126/science.1182221

Skarke, A., Ruppel, C., Kodis, M., Brothers, D., & Lobecker, E. (2014). Widespread methane leakage from the sea floor on the northern US Atlantic margin. *Nature Geoscience*, *7*(9), 657.

Sommer, S., Gier, J., Treude, T., Lomnitz, U., Dengler, M., Cardich, J., & Dale, A. W. (2016). Depletion of oxygen, nitrate and nitrite in the Peruvian oxygen minimum zone cause an imbalance of benthic nitrogen fluxes. *Deep sea research part I: Oceanographic research papers*, *112*, 113–122.

Spielhagen, R. F., Werner, K., Sørensen, S. A., Zamelczyk, K., Kandiano, E., Budeus, G., et al. (2011). Enhanced modern heat transfer to the Arctic by warm Atlantic water. *Science*, *331*(6016), 450–453. https://doi.org/10.1126/science.1197397

Steinle, L., Knittel, K., Felber, N., Casalino, C., Lange, G., Tessarolo, C., et al. (2018). Life on the edge: active microbial communities in the Kryos MgCl 2-brine basin at very low water activity. *ISME J*, *12*(6), 1414.

Steinle, L., Graves, C. A., Treude, T., Ferré, B., Biastoch, A., Bussmann, I., et al. (2015). Water column methanotrophy controlled by a rapid oceanographic switch. *Nature Geoscience*, *8*(5), 378.

Teske, A., & Sørensen, K. B. (2008). Uncultured archaea in deep marine subsurface sediments: Have we caught them all? *The ISME Journal*, *2*(1), 3.

Thatcher, K. E., Westbrook, G. K., Sarkar, S., & Minshull, T. A. (2013). Methane release from warming-induced hydrate dissociation in the West Svalbard continental margin: Timing, rates, and geological controls. *J. Geophys. Res.: Solid Earth*, *118*(1), 22–38.

Thornton, B. F., Geibel, M. C., Crill, P. M., Humborg, C., & Mörth, C.-M. (2016). Methane fluxes from the sea to the atmosphere across the Siberian shelf seas. *Geophysical Research Letters*, *43*(11), 5869–5877.

Torres, M., & Colwell, F. (2018). *Assessing the response of methane hydrates to environmental change at the Svalbard continental margin*. Corvallis, OR (United States): Rep., Oregon State Univ.

Torres, M. E., McManus, J., Hammond, D., de Angelis, M. A., Heeschen, K. U., Colbert, S. L., et al. (2002). Fluid and chemical fluxes in and out of sediments hosting methane hydrate deposits on Hydrate Ridge, OR, I: Hydrological provinces. *Earth Planet. Science Letters*, *201*, 525–540.

Treude, T. (2003). Anaerobic oxidation of methane in marine sediments, Ph.D. thesis thesis, 245, accessible at http://elib.suub.uni-bremen.de/publications/dissertations/E-Diss845_treude.pdf pp.

Treude, T., Boetius, A., Knittel, K., Wallmann, K., & Jørgensen, B. B. (2003). Anaerobic oxidation of methane above gas hydrates at Hydrate Ridge, NE Pacific Ocean. *Marine Ecology Progress Series*, *264*, 1–14.

Treude, T., Krüger, M., Boetius, A., & Jørgensen, B. B. (2005). Environmental control on anaerobic oxidation of methane in the gassy sediments of Eckernförde Bay (German Baltic). *Limnology and Oceanography*, *50*, 1771–1786.

Treude, T., Niggemann, J., Kallmeyer, J., Wintersteller, P., Schubert, C. J., Boetius, A., & Jørgensen, B. B. (2005). Anaerobic oxidation of methane in the sulfate-methane transition along the Chilean continental margin. *Geochimica et Cosmochimica Acta*, *69*(11), 2767–2779.

Vanneste, M., Berndt, C., Laberg, J. S., & Mienert, J. (2007). On the origin of large shelf embayments on glaciated margins—Effects of lateral ice flux variations and glacio-dynamics west of Svalbard. *Quaternary Science Reviews*, *26*(19–21), 2406–2419.

Veloso-Alarcón, M. E., Jansson, P., De Batist, M., Minshull, T. A., Westbrook, G. K., Pälike, H., et al. (2019). Variability of acoustically evidenced methane bubble emissions offshore western Svalbard. *Geophysical Research Letters*, *46*(15), 9072–9081.

Wallmann, K., Aloisi, G., Haeckel, M., Obzhirov, A., Pavlova, G., & Tishchenko, P. (2006). Kinetics of organic matter degradation, microbial methane generation, and gas hydrate formation in anoxic marine sediments. *Geochimica et Cosmochimica Acta*, *70*(15), 3905–3927.

Wallmann, K., Pinero, E., Burwicz, E., Haeckel, M., Hensen, C., Dale, A., & Ruepke, L. (2012). The global inventory of methane hydrate in marine sediments: A theoretical approach. *Energies*, *5*(7), 2449–2498.

Wallmann, K., Riedel, M., Hong, W.-L., Patton, H., Hubbard, A., Pape, T., et al. (2018). Gas hydrate dissociation off Svalbard induced by isostatic rebound rather than global warming. *Nature Comm.*, *9*(1), 83.

Wedepohl, K. H. (1995). The composition of the continental crust. *Geochimica et Cosmochimica Acta*, *59*(7), 1217–1232.

Westbrook, G. K., Thatcher, K. E., Rohling, E. J., Piotrowski, A. M., Pälike, H., Osborne, A. H., et al. (2009). Escape of methane gas from the seabed along the West Spitsbergen continental margin. *Geophysical Research Letters*, *36*(15). https://doi.org/10.1029/2009GL039191

Wilfert, P., Krause, S., Liebetrau, V., Schönfeld, J., Haeckel, M., Linke, P., & Treude, T. (2015). Response of anaerobic methanotrophs and benthic foraminifera to 20 years of methane emission from a gas blowout in the North Sea. *Marine and Petroleum Geology*, *68*, 731–742.

Yamamoto, S., Alcauskas, J. B., & Crozier, T. E. (1976). Solubility of methane in distilled water and seawater. *Journal of Chemical & Engineering Data*, *21*(1), 78–80.

Yao, H., Hong, W.-L., Panieri, G., Sauer, S., Torres, M. E., Lehmann, M. F., et al. (2019). Fracture-controlled fluid transport supports microbial methane-oxidizing communities at Vestnesa Ridge. *Biogeosciences*, *16*(10), 2221–2232.